
Article:
Entwistle, J., Beaucage, G. and Patwardhan, S. orcid.org/0000-0002-4958-8840 (2020) Mechanistic understanding of pore evolution enables high performance mesoporous silicon production for lithium-ion batteries. Journal of Materials Chemistry A, 8 (9). pp. 4938-4949. ISSN 2050-7488

https://doi.org/10.1039/C9TA13633A

Mechanistic understanding of pore evolution enables high performance mesoporous silicon production for lithium-ion batteries

*Jake E. Entwistle[1,2] Gregory Beaucage[3] and Siddharth V. Patwardhan[1]**

[1] Green Nanomaterials Research Group, and
[2] Centre for Doctoral Training in Energy Storage and its Applications,
Department of Chemical and Biological Engineering,
The University of Sheffield
Mappin Street, Sheffield S1 3JD, UK.
[3] Department of Chemical and Materials Engineering,
University of Cincinnati, Cincinnati, Ohio 45221, USA.
*s.patwardhan@sheffield.ac.uk

Key words: Lithium-ion battery, anode, silica, magnesium reduction, magnesiothermic reduction

ABSTRACT

The cycling of silicon anodes within a lithium-ion battery (LIB) leads to degradation and capacity fade due to the 280% volume change of silicon. Many avenues of silicon synthesis have been explored to produce nanostructures which can withstand this change in volume. Magnesiothermic Reduction (MgTR) shows significant promise over other syntheses in scalability, economic and environmental aspects for producing porous silicon nanostructures. The problem with MgTR is a lack of understanding regarding the pore evolution of porous silicon based on reduction parameters and precursor material, which in turn limits predictive design for desired applications. Here we show that the pore structure of porous silicon is strongly related to the interconnectivity of silicon crystallites. We show that the MgTR is a thermodynamically driven equilibria which determines the purity of the silicon product. Higher temperatures also cause sintering of silicon nanocrystallites. We show that it is the interconnectivity of these crystallites that determine the pore size and distribution within porous silicon. These findings apply to a wide variety of porous silica precursors and we show this mechanism is true for the introduction of pores into nonporous quartz after MgTR. Further, we show that by exploiting this mechanism, mesoporous silicon can be produced which has excellent promise for LIB applications with a capacity of 2170 mAh/g after 100 cycles. The findings herein can be taken forward to design optimal materials for LIB applications. These results strongly support the potential for reduction in silicon costs for LIB in both economic and environmental terms as well as for a reverse engineering approach to design specific porous silicon for desired applications even beyond LIB.

ToC graphic and text

A detailed mechanistic understanding of pore evolution of porous silicon is critical in developing high performance anodes for lithium-ion batteries. We find that the pore structure of porous silicon is strongly related to the interconnectivity of silicon crystallites, which enabled us to produce mesoporous silicon with a capacity of 2170 mAh/g after 100 cycles. This has potential in designing high-value porous silicon for LIB and beyond.

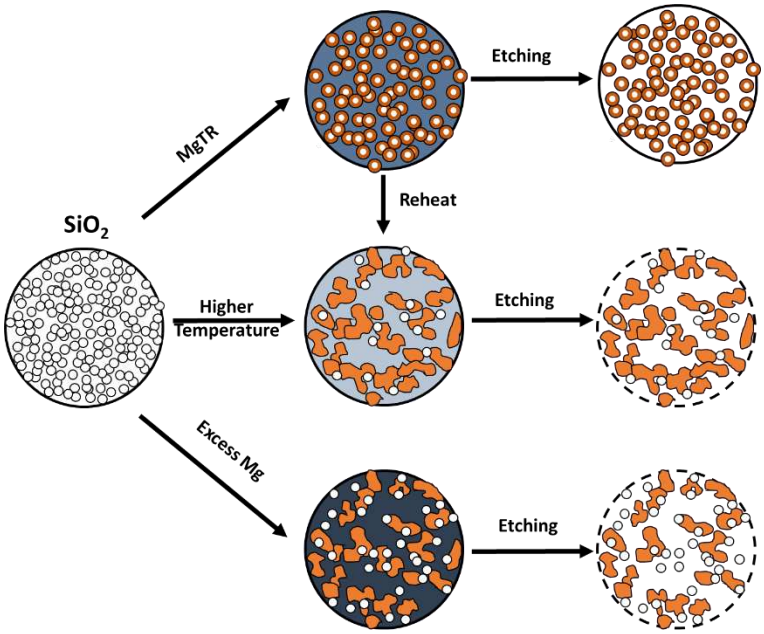

1. INTRODUCTION

The advent of the Lithium-ion battery (LIB) revolutionised portable electronics and has a key role to play in the integration of large scale renewable power and the electrification of transport. Increased energy and power density along with lower cost active materials will accelerate the adoption of LIBs in the above applications.[1]

The current commercial LIB uses an intercalating graphite anode where lithium-ions reversibly transfer within the planes of the graphite sheets resting in an interstitial site shared between six carbon atoms (C_6Li), corresponding to a 371 mAh/g gravimetric and 830 mAh/ml volumetric capacity. Silicon has a much higher gravimetric and volumetric capacity than graphite at 3580 mAh/g and 2190 mAh/ml. The high capacity of silicon arises from the formation of the lithium silicon alloy $Li_{3.75}Si$. The reversible formation of lithium silicon alloys involves the breaking and reforming of chemical bonds within the silicon structure upon every cycle. The large number of lithium-ions alloyed with silicon causes a 280% volume change. [2]

Large volume change of silicon within the constrained environment of a composite electrode leads to structural damage and isolation of active material, in turn this decreases the capacity of the cell as it cycles. This challenge hinders the incorporation of silicon into the LIB anode. Another challenge is the relatively low lithium diffusion rates within silicon, 10^{-10}-10^{-11} cm^2/s, [3],[4] compared with the range 10^{-6}-10^{-11} cm^2/s reported for graphite electrodes.[5] At higher current rates, voltage drop across the internal resistance of the battery can compound the theoretical capacity not being reached.[6] We have discussed this point in depth elsewhere.[7]

Porous silicon morphologies can address both volumetric expansion and slow lithium diffusion rates of silicon. Stress generation upon lithiation has been modelled for lithium insertion materials[8],[9] which in turn have been applied to models of lithiation in porous silicon structures. [6],[10],[11] The maximum stresses experienced in porous silicon during lithiation is significantly lower than solid silicon.[10] Additionally it has been shown that higher void fractions lead to lower induced stresses and larger pores have lower hoop stresses than smaller pores.[6] For more detail readers are directed to our recent review.[7] Ultimately porous silicon

can expand into its own pore volume, thereby limiting stresses on the material. The innate high surface area of porous silicon increases accessibility of electrolyte to silicon surfaces, shortening lithium diffusion lengths and aiding higher rate capabilities.

Porous silicon can be produced via a number of synthetic routes, such as electroless and electrochemical etching, chemical vapour deposition and ball milling, to name a few.[12],[13] However, to make an impact on a commercial scale, any synthesis route needs to be scalable, economical and desirably environmentally friendly. MagnesioThermic Reduction (MgTR) has previously been highlighted not only for scalability and potential low cost, but it can offer additional advantages, such as relatively low reaction temperatures, benign reactants and products, and a wide variety of silicon product properties.[7]

MgTR is a two-step synthesis route highlighted with Figure 1 (top); firstly, a silica template is reduced by magnesium according to Equation (1), secondly magnesium oxide and any magnesium silicide formed via a side reaction (Equation 3) are removed from the products with hydrochloric acid. The first reduction step is typically performed in the temperature range of 550 – 950 °C under an argon atmosphere. Due to the reduction temperature being lower than the melting point of silica and silicon, the correct conditions can produce silicon analogues of silica templates. The method has shown the ability to preserve intricate features as small as 15 nm.[14] Due to the vast library of porous silica available, MgTR is a powerful tool for the template assisted synthesis of a wide range of porous silicon.[15]

$$SiO_2 + 2Mg \rightarrow Si + 2MgO \qquad \text{Equation (1)}$$

$$Si + 2Mg \rightarrow Mg_2Si \qquad \text{Equation (2)}$$

$$SiO_2 + Mg_2Si \rightarrow 2Si + 2MgO \qquad \text{Equation (3)}$$

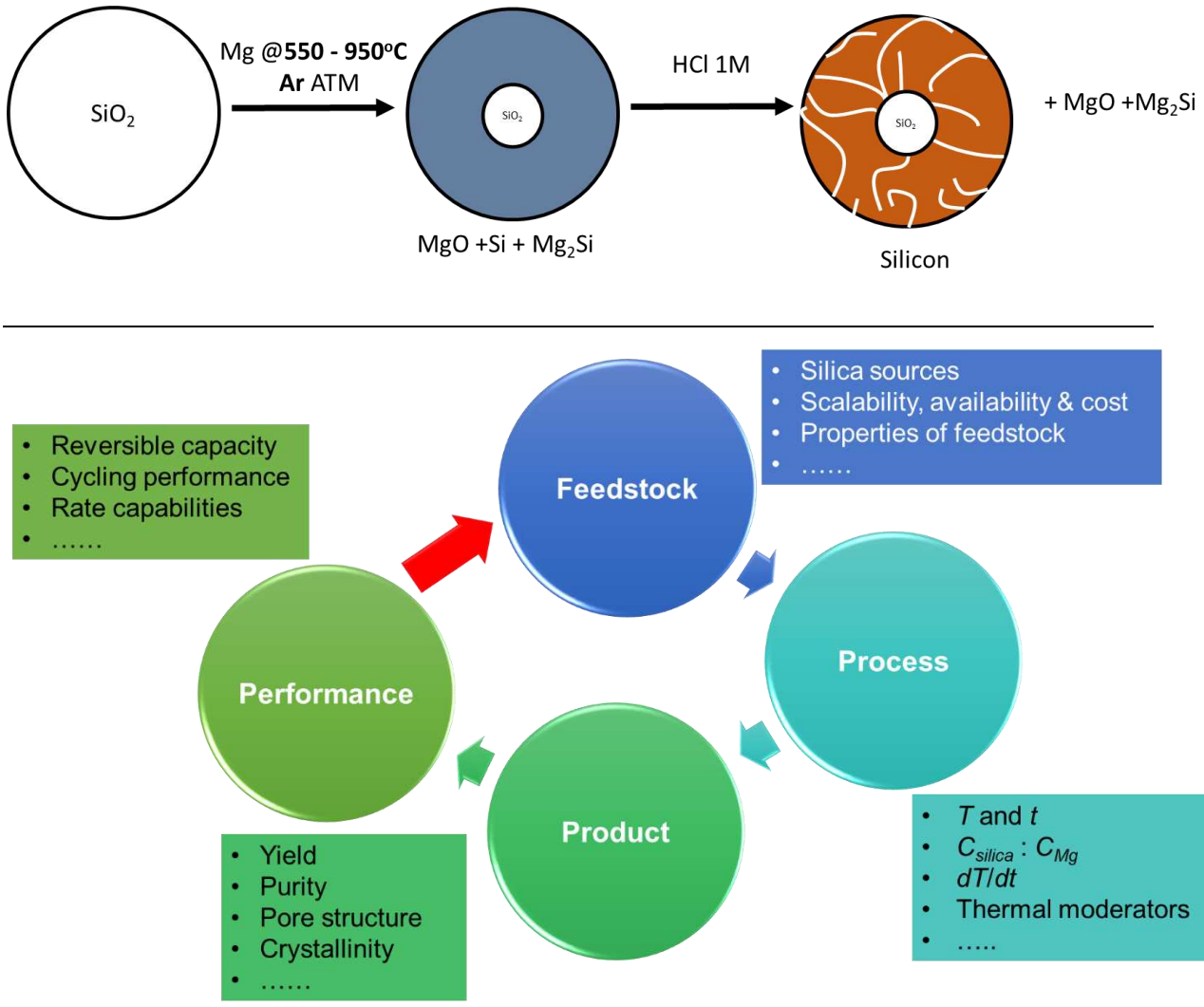

Figure 1, (Top) A schematic representations of the Magnesiothermic reduction reaction. (Bottom) A schematic showing the interconnectivity between the feedstock, the reduction process, the resultant silicon produced and its performance in LIB. The red arrow shows desired reverse engineering required to select feedstock and process for a given performance. T and t are temperature and duration of MgTR. C_{silica} : C_{Mg} is the stoichiometric ration of precursors and dT/dt is the heating rate.

The porosity of silicon produced through MgTR is a key parameter in the justification for studying these materials for LIB applications as discussed above. However complete characterisation of pore properties in silica precursors and silicon products is often lacking. It has been highlighted that MgTR conditions can have a much greater effect on the silicon properties than the silica template used.[7] Understanding of MgTR conditions and their effect on the pore properties of silicon is critical to the utilisation of these materials in LIBs, however, the underpinning mechanisms remain elusive.

There are possibly a number of factors affecting the properties and performance of porous silicon produced from MgTR (see Figure 1, bottom). It is known that pore properties of the silica template are not the only factor governing pore properties in the silicon analogue. This unexpected, as the silicon analogue generally adopts the morphology of the templating silica. However, oxygen atoms are being removed from the host, thus inevitably causing structural changes. Additionally, the product phases of magnesium oxide and silicon are interwoven with each other, this morphology is crucial to allow the complete removal of magnesia during the HCl washing.[16]

As well as pore properties, the purity of the silicon formed is critical for LIB applications. Often MgTR does not fully reduce the silica to silicon. Typically, the remaining silica has been selectively removed with toxic HF to optimise battery performance, more often than not the yield of the reduction is not stated in these cases. [7] The use of HF will add economic and environmental burden to any future development of MgTR. Recent studies have shown that small amounts of silica after reduction may be beneficial bringing into question the need for HF.[17]

Despite the aforementioned scattered investigations, currently a detailed understanding of the evolution of pore properties during the MgTR reaction is lacking. For example studies may report reaction times above 2 hours have no effect on increasing the silicon yield, [18][19] but the specific effect on pore properties and surface area evolution have not been studied.[7] Likewise a variety of molar ratios have been studied however the effect of stoichiometric ratio on the pore properties and surface area of porous silicon has not been investigated.[7] The effects of feedstock (silica) properties and the MgTR process on the properties and the performance of porous silica produced are unknown. This stops a predictive design of a method to produce mesoporous silicon structures for lithium-ion battery anodes (see the red arrow in Figure 1, bottom). In this study, we aim to address this gap in our knowledge by systematically investigating the effect of reaction conditions (time, temperature and stoichiometry) and the silica precursors on product pore properties and purity. The anode performance of silicon thus

produced will be assessed in order to understand the interconnections between feedstock, MgTR process, product and performance as shown in Figure 1 (bottom). Specifically, herein we systematically study the MgTR reaction conditions and for the first time provide an in-depth analysis of how key reaction parameters affect the pore properties of the MgTR products, which in turn affect the electrochemical performance. A key expected outcome is the understanding of pore evolution in silicon, which can help design MgTR process for desired product attributes.

2. RESULTS AND DISCUSSION

The silica used for this study is produced in house via a well-established bioinspired synthesis route.[20] The choice of silica precursor will have a significant effect on the economic and environmental impact for development of this technique at an industrial scale. Bioinspired silica is synthesised in water and at room temperature in minutes, it has shown promising scalability and economic feasibility.[21][22] Additionally the properties of the silica can be modified by changing the catalytic additive and by post/pre-treatment of supernatant.[21] The bioinspired silica produced in this study (from now on referred to as BIS, see Experimental section for details) is fully characterised in Figure S 1. The BIS is comprised of secondary particles with an average diameter of ~330nm, it has been shown previously these secondary particles are comprised of smaller primary particles of smaller diameter (discussed in section 2.2).[23] The BIS has micro and small mesoporosity which arises from the interstitial space between these primary particles.[24]

2.1 Exploring the effect of key parameters

Before systematically studying MgTR process by exploring the effects of the reaction time, temperature and the stoichiometry of the reactants, we present results from a typical MgTR experiment. Figure 2 presents the characterisation of typical porous silicon after MgTR of BIS. Figure 2a shows a Type IV isotherm indicative of a mesoporous material. Desorption branch fitting with the Barrett-Joyner-Hallenda (BJH) model provides the pore size distribution (Figure 2b), confirming mesopores with average pore size of 13 nm (also see Table S2). The formation

of crystalline silicon from MgTR was observed using XRD (Figure 2c), which also confirmed that magnesia and magnesium silicide are present after the reduction and shows that both species are completely removed during the acid washing. It has been shown previously that potential side reactions may also lead to the formation of magnesium silicates, however, no magnesium silicates were observed in this study. We note that this is the first report of mesoporous silicon production using BIS and it has it has technological advantages due to scalable, economical and sustainable nature of BIS.[25]

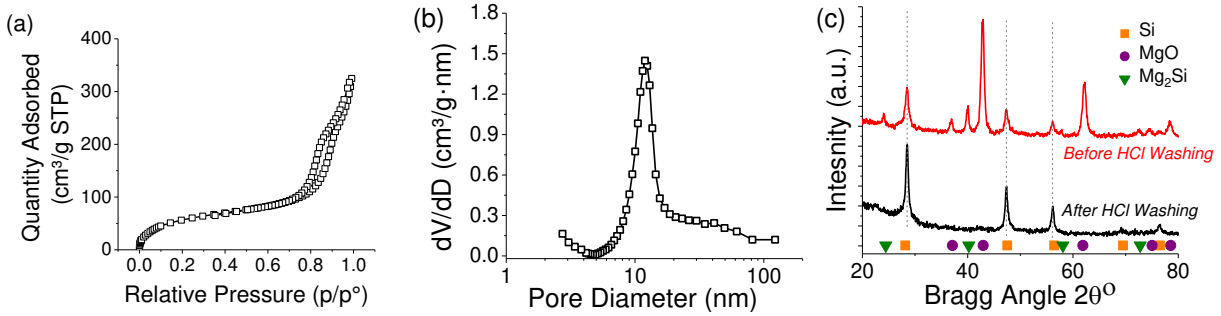

Figure 2 (a) N_2 absorption isotherm, (b) BJH pore size distribution of porous silicon product of BIS reduced for 6 hours at 650 °C with a stoichiometric ratio of 2.5:1 ($Mg:SiO_2$). (c) XRD of reaction products before and after HCl washing.

When the effect of reduction time was investigated, Figure S 2 shows that 1-hour reaction time had produced mesoporous silicon and average pore diameters around 10 nm. For longer reduction times, the porosity (pore sizes, pore volumes, specific surface areas) and the silicon crystallite sizes (obtained from Scherrer analysis of the diffractograms) did not significantly change between 1-10 hours (Figure S 2 and Table S2). Consistent with previous studies it was found that reaction time between 1 and 10 hours did not significantly affect the silicon yield with all products comprising of 57-65% silicon. We determine that reduction times longer than 1 hour do not significantly affect the silicon/silica composites produced, in terms of purity, pore properties and crystallite size.

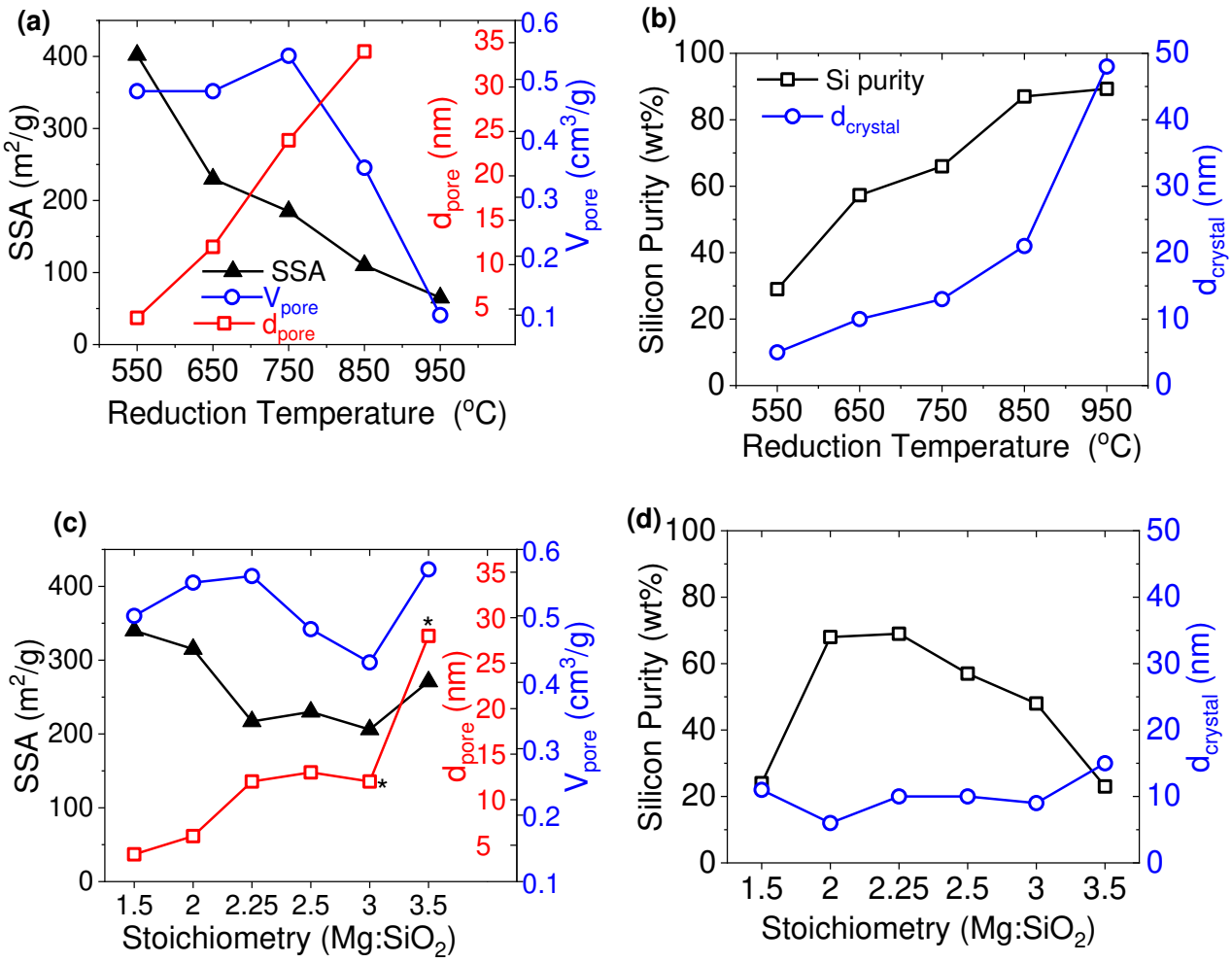

Figure 3. Effect of reduction temperature performed at a 2.5:1 Mg:SiO_2 stoichiometry (a, b) and feedstock stoichiometry at reduction temperature of 650 °C (c, d). On (a, c) BET specific surface area (SSA), BJH pore volume (V_{pore}) and average pore diameter (d_{pore}) and (b, d) silicon purity and crystallite size. * Represents bimodal distribution of pore diameters for samples reduced at 3:1 and 3.5:1 Mg:SiO_2 (see Figure S4 for pore size distribution).

As the MgTR temperature is a key parameter controlling the reaction pore evolution, it was investigated next. The onset of reduction reaction is known to take between 400 and 540 °C depending on the silica source used.[26],[27] Therefore a lower limit of 550 °C was selected for this study into reduction temperature. The reduction temperature had a significant effect on all aspects of product silicon properties. Figure 3 (a) shows a decrease in surface area from 400 to 65 m^2/g over the temperature range. The overall pore volume remained unchanged between 550 °C and 750°C at 0.50 cm^3/g, which decreased to 0.35 and 0.10 cm^3/g respectively for reaction temperature of 850 and 950 °C. The trend in surface area is related to the pore

sizes. Smaller pores contribute a higher surface area for the same overall pore volume. Therefore, the increase in pore diameter and decrease in pore volume lead to the lower surface areas observed for the samples reduced at higher temperatures. This evolution of porosity with MgTR temperature is of great importance and it is discussed in detail below (section 2.2). The purity of silicon product linearly increased from 29-87 wt% from 550 – 850°C (Figure 3 (b)) and then between 850-950 °C it begins to plateau. A clear correlation was observed between the reduction temperature and the increase in pore diameters of silicon from 4 nm at 550 °C to 34 nm at 850 °C (Figure 3 (a))

The purity of silicon increased with the temperature. At high temperatures (>850 °C), any magnesium silicide formed, gets converted to silicon via Equation (3) (see Figure S 3c), and is consistent with the literature.[27] Temperatures <850 °C are not sufficient enough to fully convert the silicide and hence they can be observed in the XRD results (before acid etching). The average crystallite size increased from 5 nm to 48 nm across the temperature range (Figure 3b), mainly due to sintering at higher temperatures. Although this produced purer silicon at higher temperatures, sintering resulted in the loss of porosity. This suggests that MgTR temperature between 750 and 850 °C can provide an optimum between high porosity and high purity.

The MgTR of silica has a stoichiometric ratio of 2:1 Mg:SiO_2 if the reaction progresses without any side reactions (see Equation (1)). However, side reaction and the formation of magnesium silicide usually decreases the silicon yield and perhaps affects the porosity. In order to study this effect, we varied the Mg:SiO_2 ratio from 1.5 to 3.5 and the results are shown in Figure 3c, d and Figure S 4. Increasing the stoichiometric ratio from 1.5 – 2.5:1 increased the pore sizes from 4 nm to 13nm, but maintained the size distribution profile. Increasing the stoichiometric ratio to 3:1 resulted in a bimodal distribution of mesopores. The pores cantered around 13 nm decreased with a significant increase in larger mesopores (>10 nm). Increasing the stoichiometric ratio further to 3.5:1 resulted in even broader distribution of pores between 10-100 nm. Throughout this broadening of mesopore size distribution, pore volumes and surface

areas did not show any dramatic changes unlike those seen when the MgTR temperature was varied (Figure 3c). The yield of the silicon formed increased between 1.5 and 2.25:1 stoichiometry from 24 to 69 wt%. Increasing the stoichiometry further decreased the yield of the silicon back to 23 wt% for the 3.5:1 ratio (Figure 3d). As excess magnesium is available (>2.25:1), the side reactions of the formation of magnesium silicide reduces the yield of silicon (Figure S 4c). Interestingly, the stoichiometry did not have any significant effect on the sizes of the silicon crystals, which remained between 10-15 nm.

In summary the temperature affects the purity and silicon crystal sizes via sintering, which in turn affects the porosity. Stoichiometry of the reduction also has a significant effect on the formation magnesium silicide by-product, which affects the purity and the pore network of silicon formed. It is clear that the reaction chemistry and the processing conditions affect the properties of silicon, where the porosity and purity are interlinked with the crystallite size and the by-products formed. In the next section, we aim to reveal these interdependencies by providing a mechanistic understanding.

2.2 Understanding Magnesiothermic Reduction

Our results show that the two key factors affecting the porosity, the purity and (potentially) the morphology of silicon produced from MgTR are the silicon crystal size and the amount of magnesium silicide (Mg_2Si) by-product produced. We propose a mechanistic view that connects the MgTR process conditions to the physicochemical properties of silicon via the silicon crystal sizes and Mg_2Si formation (see Figure 4). Below we explain this mechanism by discussing the roles of both the silicon crystal size and Mg_2Si in porous silicon formation.

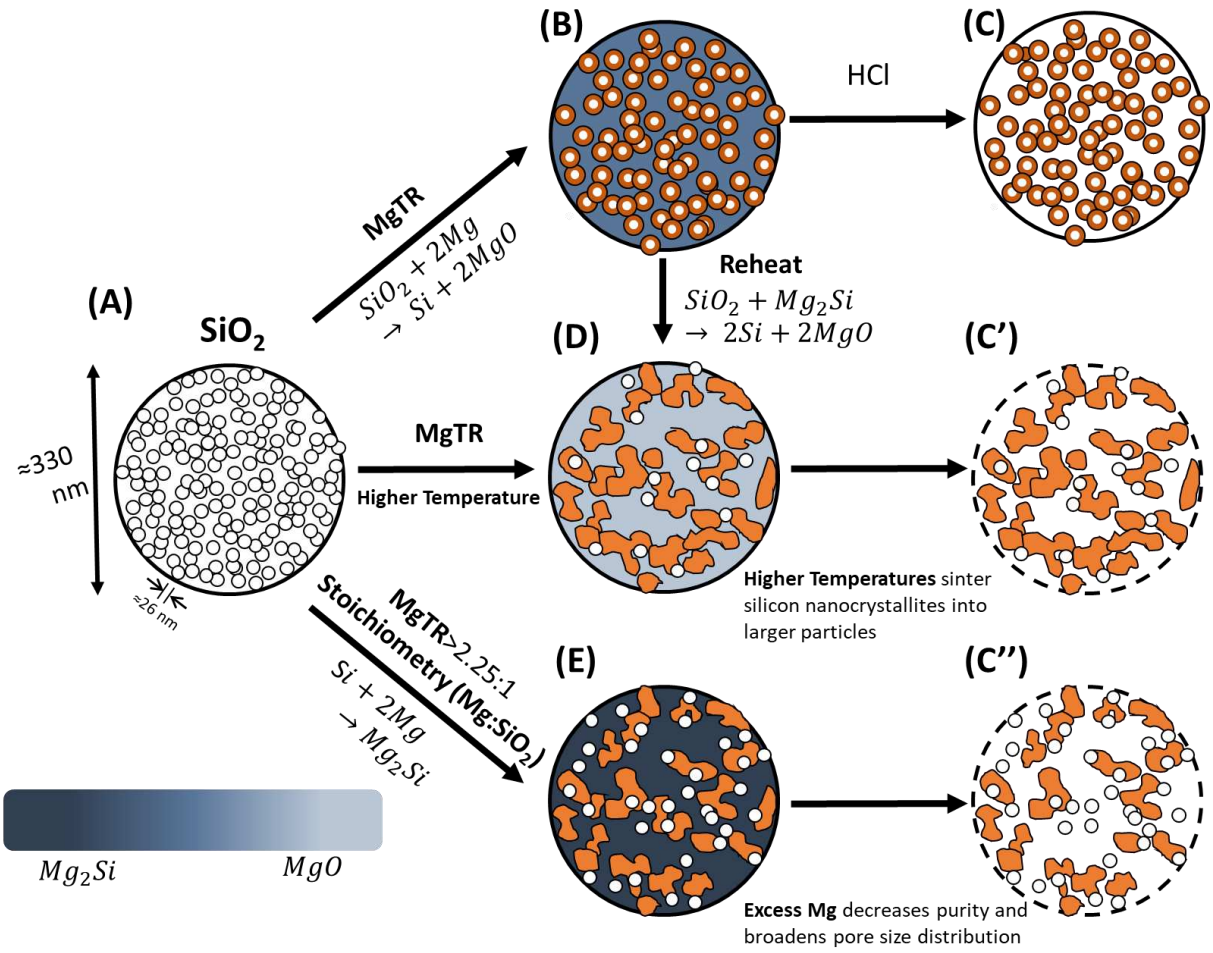

Figure 4. A schematic showing the formation and evolution of silicon crystals (C, C' and C'') from precursor BIS silica and the effect of temperature and stoichiometry on pore evolution. White particles with black outlines show primary silica particles. The dark black outline indicates a secondary particle. Orange colour denotes pure silicon nanocrystals. Other products (MgO, Mg_2Si and their mixture) are shown in shades of blue corresponding to the colour bar shown in the bottom left – darkest blue represents pure Mg_2Si and the lightest MgO (any colour in between represents a mixture of these two products).

The role of Si crystal size in controlling porosity

Characterisation of BIS using SEM and USAXS reveal that it is a hierarchically structured material with primary particles of ~26 nm, which aggregate to form secondary particles ~330 nm (Figure 5a, d and Table S 3). These features are depicted in Figure 4A. As observed from the results above, the same starting materials (BIS in this case, Figure 4A) produces widely varying porous silicon as shown in Figures 2, 3 and S 2-4. We propose that this transformation of primary silica particles within the secondary particles occurs from the surface to the core (see the core-shell particles shown in Figure 4B). The temperature of MgTR controls the extent

of this conversion, while the removal of oxygen (via MgO) from silica creates mesoporosity (Figure 4C). Higher temperatures of MgTR (>750 °C) induce sintering of silicon nanocrystals (Figure 4D), while also increasing the purity of silicon. The sintering leads to large crystals and concomitant reduction in porosity (Figure 4C'). This is a key finding, especially because it can enable monitoring/controlling MgTR by measuring silicon crystallite size as a suitable measure of product quality. This mechanism is explained below by focusing on the morphology and the crystallite sizes.

For MgTR temperatures up to 750 °C, the spherical morphology of the BIS secondary particles appears to be maintained throughout the reduction (Figure 5 and Figure S 5), while also showing 'speckles' on these particles. The sample produced at 750 °C shows that the parent ~330 nm spherical particles with constituent smaller crystallites (Figure 5c). This observation is supported by the Scherrer analysis, which shows the silicon crystallites sizes systematically increase from 5 nm to 48 nm (Figure 5d) as the MgTR temperature is increased (also see their schematic representation in Figure 4C and C'). When these particles are large enough (>10 nm), they are also visible via SEM (e.g. for MgTR temperature ≥750 °C). These speckles are likely to correspond to the silicon crystallites and as the MgTR temperature is increased, more silica is reduced to silicon, thereby increasing these features. USAXS results also show that the primary particles between 17-71 nm are present (Figure 5(d)), which represent the primary silica particles from BIS as well as the silicon crystals. As USAXS cannot discriminate between silicon crystals and silica particles, the measurement covers both components. As samples reduced at 550 and 650 °C contain 40-70% of unreacted silica, USAXS measurements are overshadowed by the combination of silicon crystallites and silica particles, hiding the silicon crystals. For sample produced at 850 °C, although the silicon crystallites are clearly visible by SEM (21 nm, see Figure S 5), the parent particles of ~330 nm begin to disappear. This is caused by higher conversion of silica to silicon and of sintering of silicon crystals. As this sintering continues at 950 °C, the parent particles disappear almost completely and all we can see is the 48 nm silicon crystals and fused (much larger) particles (Figure S 5), leading to a

loss of porosity. These results help explain the observed trends with porosity, purity and silicon crystal sizes shown in Figure 3.

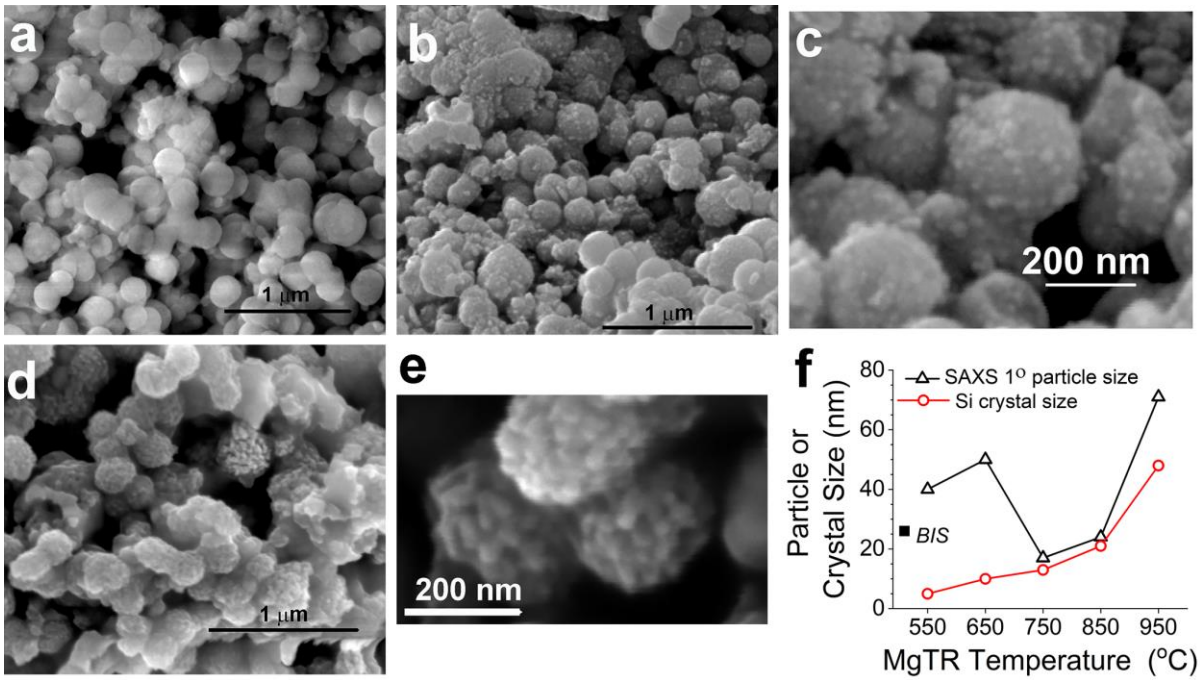

Figure 5. *SEM images of (a) unreacted feedstock BIS, and porous silicon reduced at temperatures (b-c) 550 °C and (d-e) 750 °C. (f) A comparison of primary particle size obtained from USAXS and crystallite size obtained from XRD for mesoporous silicon samples reduced between 550-950 °C. See Figure S 5 and Figure S 6 for full details.*

The effect of Mg_2Si on pore evolution

The stoichiometry ($Mg:SiO_2$) also controls the process by affecting the production of Mg_2Si by-product (Equation 2). The purity of silicon can be maximised by using an optimum stoichiometry thereby minimising the formation of Mg_2Si. However, as Mg_2Si is removed by etching (acid washing), it also affects the porosity. In order to test the role of Mg_2Si in the entire process, we performed additional experiments as follows. $Mg:SiO_2$ ratios of >1.5:1 were explored at MgTR temperatures of 650 and 850 °C. As reported above in Figure 3d (and replotted in (Figure 6a), for MgTR at 650 °C, the higher $Mg:SiO_2$ stoichiometry leads to loss in purity from the side reaction producing Mg_2Si by-product. This loss in purity arises from the increased formation of Mg_2Si (Figure 6b). However, for the same stoichiometries at 850 °C, the purity changes only slightly due to marginal changes to Mg_2Si formation. These results

strongly support that the conversion of Mg_2Si (Equation 3) is responsible for increasing silicon yield at higher temperature and that a temperature >650 °C is required to drive this conversion.

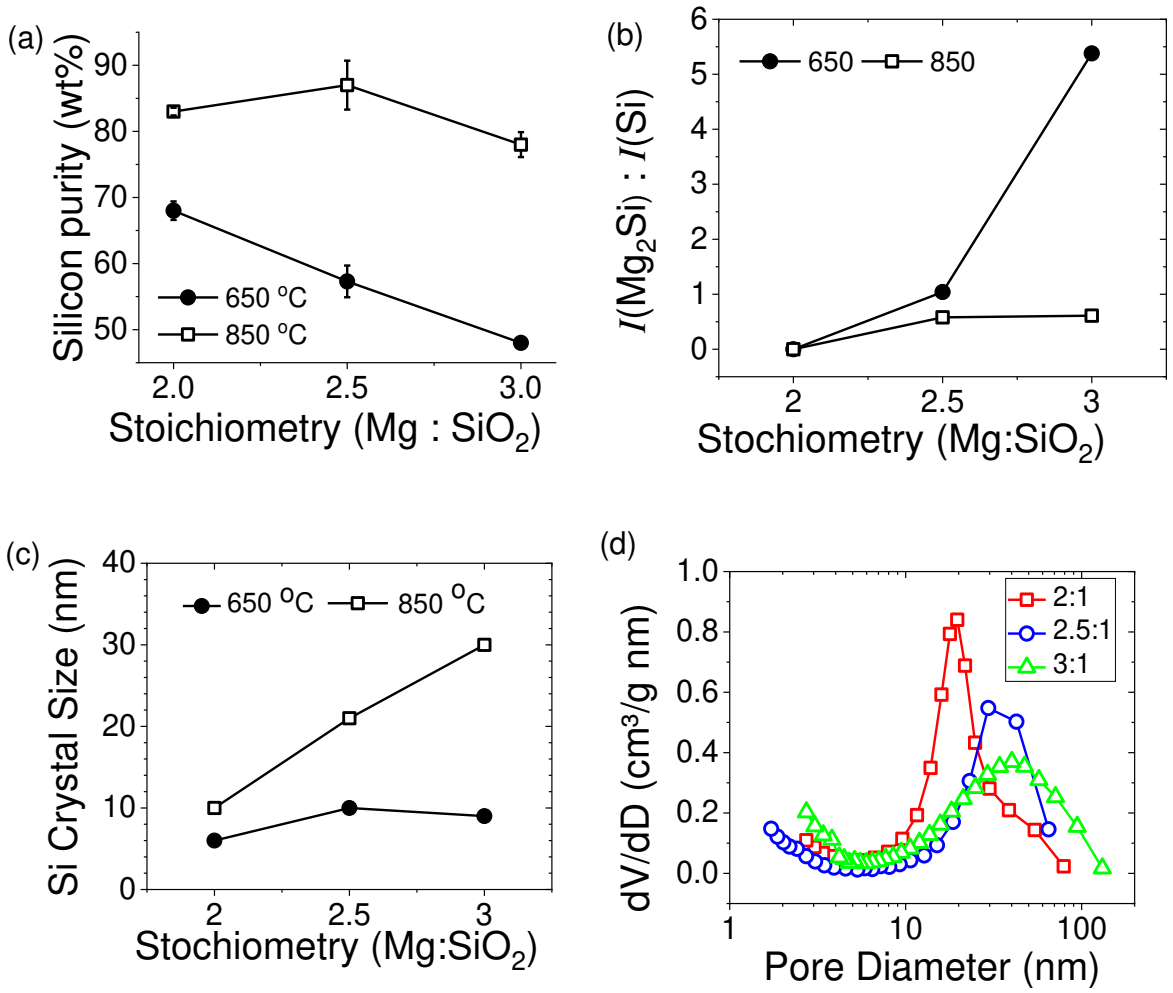

Figure 6. Silicon produced at stoichiometric ratios 2,2.5,3:1 for reduction temperatures of 650 and 850 °C (a) purity of product (wt%). (b) ratio of Mg_2Si to Si peaks in pre-acid washing XRD (c) crystallite size (d) BJH pore size distribution.

The Mg_2Si formed at high Mg: SiO_2 ratio for MgTR at 850 °C, which converted to silicon, leads to large increases in the silicon crystal size (from 10 nm at 2:1 to 30 nm at 3:1, see Figure 6c) as well as a broadening of pore size distribution (Figure 6d). This suggests that at high temperature, the silicide appears to be an *intermediate* rather than a by-product. These observations are consistent with the mechanism proposed in Figure 4 (see the conversion of A to D to C' and A to E to C'').

In order to further verify this mechanism, we produced two additional samples as follows. Firstly, a sample called *650-E-850* was prepared by performing MgTR at 650 °C for 6 hours and then cooling it to room temperature. The sample was then etched with acid to obtain porous silicon; this silicon was then heated to 850 °C for 6 hours and cooled to room temperature for analysis. Secondly, *650-850* was prepared similar to *650-E-850*, but without any acid etching (Figure 4 pathway B to D). The *650-E-850* sample appeared to be identical to the sample reduced at 650°C (see no change in the purity, silicon crystal size, pore volume or the pore size distribution in Figure S 8 and Table 1), while very different to the sample prepared at 850°C. This clearly suggests that once the Mg_2Si was removed, there was no further change in the sample, even upon heating to higher temperature, further confirming that the silicide is an intermediate rather than a by-product. This observation, along with the increase in silicon yield for the *650-850* sample compared to the 650 sample, means that at high MgTR temperatures, the predominant reaction occurring is the reaction Equation 3 (the conversion of silicide to silicon). Further, the *650-850* sample appears to be similar to the sample prepared directly at 850°C. Noting that *650-850* sample was reduced for 6 hours at each temperatures (12 hours in total), while the sample prepared directly at 850°C was reduced only for six hours, it further supports that the purity of the silicon produced via MgTR is thermodynamically and not kinetically limited.

Table 1. The effect of removal (or not) of Mg_2Si intermediate. A stoichiometry of 2.5:1 and reduction time of 6 hours in each step was used. 'E' denotes etching via acid washing. Full results are shown in *Figure S 8*. PV= Pore volume APD=Average Pore Diameter.

Sample	BET SSA (m^2/g)	BJH PV (cm^3/g)	APD (nm)	wt% Si	Si_{Cry} Size (nm)
650	230	0.48	12	57	10
850	110	0.35	34	87	21
650-E-850	155	0.42	14	59	11
650-850	107	0.24	38	79	25

In summary, in this section, we have shown how the silicon crystal size and the formation/ conversion of Mg_2Si control the critical quality attributes of silicon produced (Figure 4), such as the purity and the porosity (surface area, pore volume and pore size distribution). We have also shown how these features relate to the MgTR conditions; by exploiting this knowledge, we were able to produce porous silicon with widely varying properties from a single feedstock (BIS in this case). In order to further validate the utility of this mechanism, below, we present the results from using a range of silica feedstocks for producing silicon via MgTR.

2.3 Extending the mechanism to other precursors

The mechanism proposed in Figure 4 suggests that the arrangement of the primary silicon nanocrystallites and their formation are the critical factors determining the pore properties of the product. Although we have shown this to be the case for one type of silica (BIS), here we test this mechanism for alternative silica precursors, in particular silica precursors which initially do not have a hierarchical structure or are not porous. Therefore, we selected following three commercial grade silicas (precipitated silica, silica gel and porous silica) and quartz. Note that these silicas are not known to exhibit hierarchical structures that are seen for BIS and that quartz did not contain any porosity (see Figure S 9). These silica precursors with varying initial porosities were reduced at 650 and 850 ^oC to study the effect of silica precursor properties on the silicon purity porosity.

As shown in Figure 7 (and also in Figure S 10 and Table S 6) without exception, each precursor produced mesoporous silicon, irrespective of the porosity (or not) of the precursors. This clearly highlights that the porosity of the feedstock silica does not control the porosity of silicon produced upon MgTR. The silicon crystal sizes, the porosity and purity of silicon produced from these different silicas were examined (see Figure S 10 and Table S 6). The trends observed with respect to the MgTR temperature were in full agreement with those reported for BIS above and the mechanism proposed in Figure 4. For example, the silicon crystal sizes were always larger for MgTR performed at 850 ^oC compared to 650 ^oC.

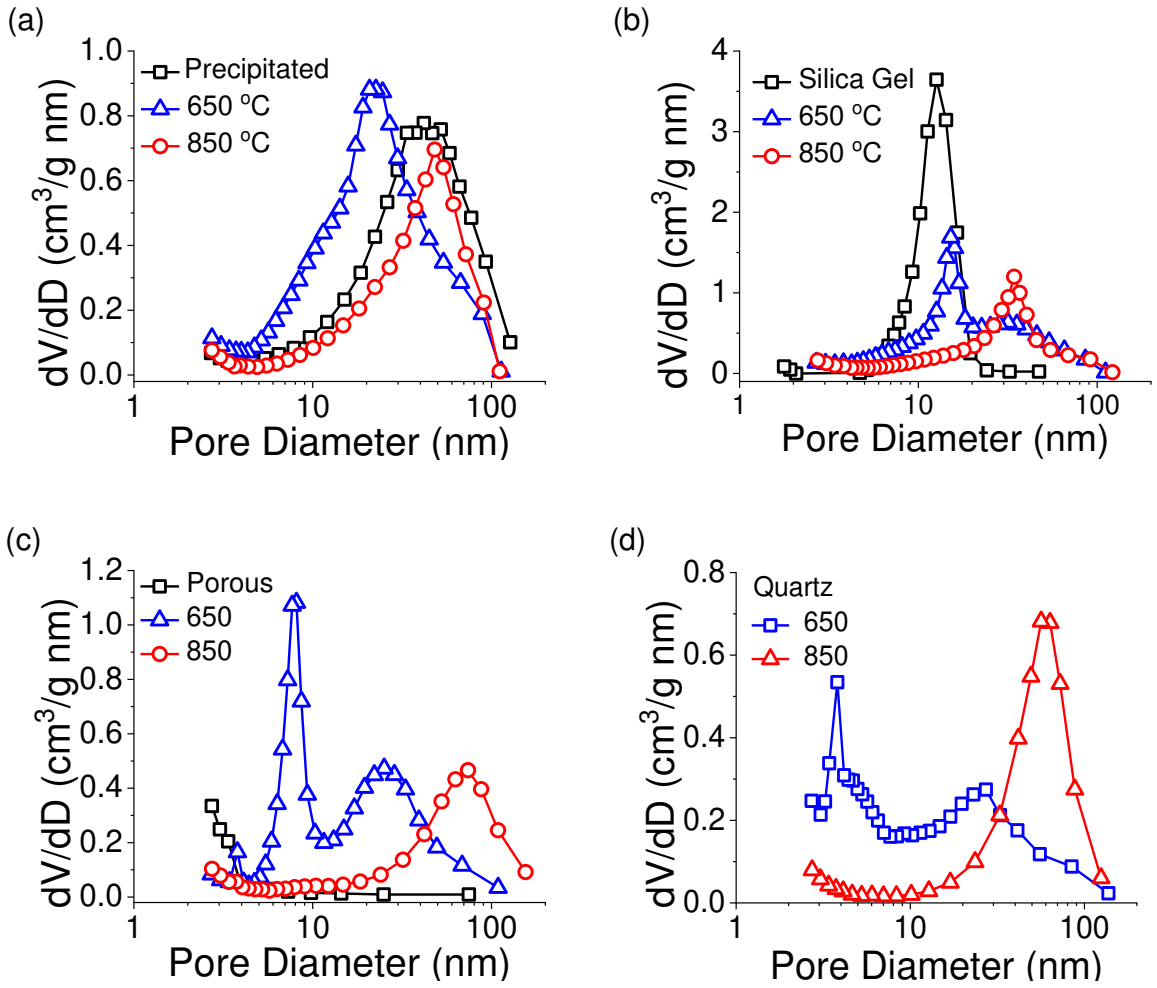

Figure 7. BJH pore size distributions of silica precursors before and after MgTR at 650 and 850 °C.

Of particular interest is the reduction of the non-porous and crystalline quartz precursor. Although quartz[28],[17] and other non-porous precursors[29] have been reduced to silicon via MgTR before, by thorough characterisation, we are able to demonstrate a relation between the silicon nanocrystals and the porous nature of the reduction products. In the case of non-porous quartz, the pores in the product can only be produced as a result of the MgTR, the formation of silicon nanocrystallites and the removal of magnesium oxide from around these crystallites. This introduction of mesoporosity (and some macroporosity) in a non-porous quartz sample supports the pore formation mechanism proposed in Figure 4. In this quartz-derived structure, all pores are a result of silicon nanocrystals forming during the MgTR process and corresponding loss of oxygen atoms via MgO.

The meso- and micro-porous precipitated silica is also of interest, as the yield for this sample did not increase as significantly between 650 and 850 °C as the other precursors, just +6%. However, the crystallite size did increase from 8 to 19 nm respectively, as expected from sintering of crystallites at higher temperatures. Due to the increase in crystallite size, the pore size distribution increased form a centre at 22 to 50 nm. This finding fits with our presented hypothesis of the relation between crystallite size and pore size distribution in this sample where despite only a small increase in purity, the pore size changed due to the increasing silicon crystal size.

These experiments reinforce the key findings from the above study on BIS and crucially that they apply to a wide variety of porous and non-porous silica sources: Firstly, the overall purity of the silicon product, governed by the extent of the MgTR reaction, is increased by increasing reduction temperature. Secondly, performing MgTR at higher temperature causes sintering and increase in silicon nanocrystal size. Finally, and linked with the findings above, the introduction of silicon nanocrystallites leads to porosity within the product and the size of these mesopores is strongly related to the silicon crystallite size as well as Mg_2Si formation. The introduction of mesopores into reduced quartz exemplifies that initial porosity within the template silica structure is not necessary to produce a porous silicon product. Instead this sample shows that the silicon nanocrystallites produced form a porous structure, and the size and distribution of these crystallites determines the pore properties formed.

2.4 Performance of porous silicon in LIB

Magnesiothermic reduction is touted for its ability to produce porous silicon as a highly attractive synthesis route for porous silicon anode materials. For the first time we have presented a detailed understanding of the nature of porous silicon structures produced from the MgTR. Below therefore we present the anode performance of these porous silicon.

One striking feature of many reports on MgTR is the use of hydrofluoric acid (HF) in the selective removal of silica from the porous silicon produced. The use of HF adds a second synthesis step, a step with particular environmental and economical drawbacks if MgTR is

ever to be commercialised. We therefore choose to present the anode performance of porous silicon produced from MgTR without the use of HF.

Silicon produced at temperatures ranging from 550-950 °C have a wide range of purity and pore properties. The capacities of these porous silicon samples are displayed in Figure 8 (a). The low purity of 29 wt% Si produced at 550 °C had an initial capacity of 830 mAh/g; after 100 cycles only 16% of this initial capacity was lost. Although this capacity is the lowest of the study, the capacity was still more than twice the theoretical capacity of graphite and retention over 100 cycles is excellent (compare this with the -325mesh silicon, which showed 94% capacity fade to 150 mAh/g after 40 cycles, see Figure S 16). The initial capacities of the samples produced at 650 and 750 °C were 1770 and 2080 mAh/g respectively. After 100 cycles the capacity of both samples faded by 39% and 59% respectively. The 850 °C reduced sample shows the highest initial capacity of 3270 mAh/g, and also shows good capacity retention of 2170 mAh/g after 100 cycles. The 950 °C sample has a high initial capacity of 2990 mAh/g due to its high purity of 89 wt%Si but shows a rapid and significant capacity fade after 100 cycles of 75% reaching a final capacity same as that recorded for the 550 °C reduced sample. The capacity fade of these porous and non-porous silicon structures is likely to follow the well-known mechanisms reported in the literature, which include pulverisation of silicon crystallites, electrode degradation and continual SEI formation.[30],[31] The matter of continual SEI formation is clear from Figure S14 and is discussed further below. Without exception these silicons show greatly increased stability than commercially available -325mesh silicon particles (Figure S 16).

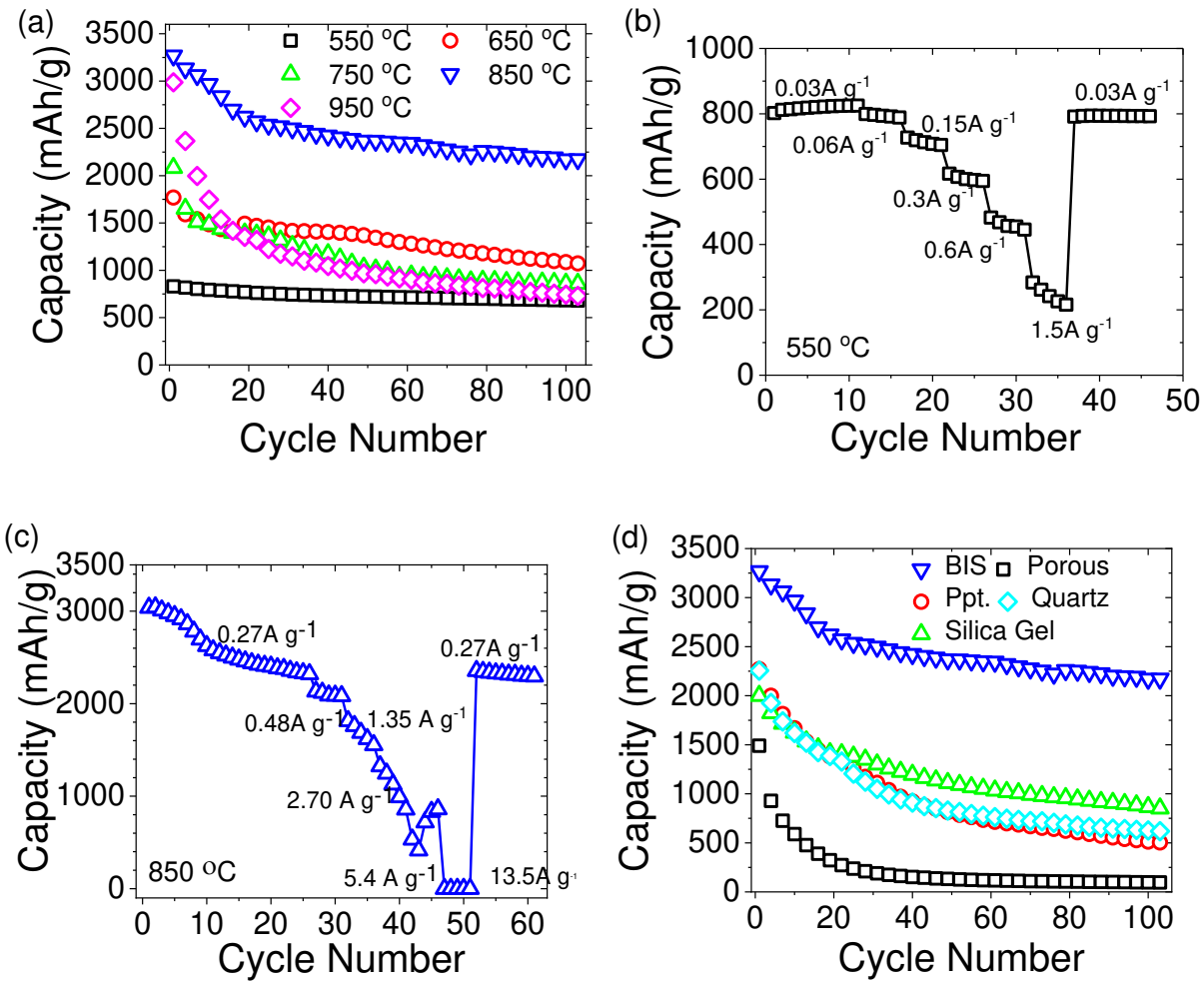

Figure 8. Discharge capacity of porous silicon/silica composites reduced between 550-950 °C from (a) BIS and The rate capabilities of porous silicon reduced at (b) 550 °C and (c) 850 °C. (d) other silica precursors reduced at 850 °C.

For the 550 °C sample, the good capacity retention is attributed to the inactive silica component. This silica can act as a scaffold to buffer the volume expansion of silicon between cycles. As the wt% of silicon in the samples increases, the initial capacity increases, however the stability is significantly affected by reduced amount of silica. It is hypothesised that as the amount of silica in the sample decreases, the scaffolding effect is reduced and the silica present hinders the capacity retention. Significant improvement on the initial capacity and cycling of the sample produced at 850 °C is attributed to a combination of a step change in both its purity (from 66% for 750 °C to 87%) and nanocrystal size (from 13 nm at 750 °C to 21 nm), while retaining mesoporosity. The larger diameter mesopores experience smaller hoop stresses around the surface of a pore as it expands.[6] The larger mesopores of the 850 °C

sample are therefore better suited to buffer the stresses of Si volume expansion upon cycling. These properties suggest an optimum in terms of electrochemical performance. The initial fading of the capacity in first 20 cycles is most likely from the destruction of 13% silica present.

The porous nature of the composites is also playing a significant role in the capacity and cyclability of these materials. This is clearly shown in the difference between the 850 and 950 ^{o}C reduced samples. Both samples have similar purities of 87 and 89 wt% silicon respectively, the 850 ^{o}C sample contains mesopores and small macro pores whilst the 950 ^{o}C sample does not (Figure S 3(b)). The non-porous silicon has a rapid and catastrophic capacity fade in the first 10 cycles.

In order to further probe the electrochemical process, in particular lithiation and delithiation of silicon during cycling, differential capacity plots are presented (Figure S 13). The differential capacity plots show similar characteristics across the range. The disappearance of the sharp cathodic peak at 0.43 V in the first 10 cycles corresponds to the delithiation of the silicon of the highest lithiated state (c-$Li_{3.75}Si \rightarrow$ a-$Li_{1.1}$ Si) the disappearance of this peak during cycling suggests an increase in electrode resistance as cycles progress.[32],[33] These high surface area, porous silicon samples inherently lead to a larger formation of solid electrolyte interphase (SEI), this is reflected in the low initial columbic efficiencies (CE, see Figure S 14 (a)). The low CE in the initial cycles of the electrodes indicate a large amount of SEI formation. In addition, the unstable CE over protracted cycles (Figure S 14 (b)) is indicative of continual SEI formation or isolation of active material in the electrode. The 750 and 950 ^{o}C reduced samples have volatile CE across the 100 cycles further highlighting the instability of these active materials and indicating the breakdown from expansion and contraction which exposes virgin surfaces. The other samples have much more stable trends towards high CE at 100 cycles (99.5%) suggesting minor damage to the SEI and/or a thickening of the layer. The differential capacity plots ((Figure S 13) show shifting of anodic peaks to lower voltages between 50 and 100 cycles and cathodic peaks vis-versa, this is consistent with an increase in internal resistance of the cells caused by a thickening of the SEI. The voltage profiles (Figure S 15) show the voltage

plateau ~100mV during the first lithiation of crystalline silicon, thereafter each cycle shows the typical hysteresis of voltage profile during charge-discharge.[34]

The rate capabilities were tested for the 550 and 850 °C reduced samples (Figure 8 (b-c)).The C-rates were calculated based on the active silicon content of the material therefore are expressed in A g^{-1} to allow easy comparison. Previous studies have shown an upper limit for commercial graphite electrodes of 4C above which substantial electrode breakdown occurs (for graphite 4C = 1.48 A g^{-1}).[35] The 550 °C silicon had excellent rate performance and provided 215 mAh/g of capacity at the upper limit used for conventional electrodes, the electrode shows excellent ability to return to its initial capacity when charging rate is reduced (*Figure 8*(b)). Due to the higher silicon content in the 850 °C sample, higher charging rates were attempted. This electrode showed poor ability to handle rates >0.48 A g^{-1} and maintain high capacity. After subjecting the 850 °C electrode to extreme charging rates, the electrode is still able to return to its original high and stable capacity showing the materials robustness.

The electrochemical performance of porous silicon produced from the alternative silica precursors was also assessed and presented in Figure 8(d) (for samples reduced at 650 °C see Figure S 11). The higher purity of the silicon produced at 850 °C resulted in higher capacity of electrodes for silicon obtained for all feedstocks used herein. However, the initial capacities and the stability over 100 cycles for the BIS silicon were much higher when compared to other silicon samples produced herein. This is interesting because silicon samples produced from silicas other than BIS did contain high purities (~80%) and mesoporosity (Table S 6) the primary difference between these silicon and the BIS being the secondary particle structure. The hierarchical structure of the BIS template and hence silicon analogues as described in detail above is responsible for the better electrochemical performance of BIS. The small <370nm size of the secondary particles coupled with their porous network allows for shorter lithium diffusion pathways during cycling and an access to higher capacities.

For the application of silicon in LIB anodes, nano-structuring of the active material is often accompanied by other tools for improving capacity fade. Examples of this are tailored binders,

carbon coating of silicon and/or carbon silicon composite formation, electrolyte additives for more stable SEI formation. In our study we present the raw porous active material with carboxymethylcellulose binder and cycled with 10wt% fluoroethylene carbonate electrolyte additive, both of which have been shown to increase cyclability in silicon electrodes.[36],[33] The aerial mass loading was 0.3-0.5 mg/cm^2 of silicon active material. For high capacity electrodes this will have to be increased in future experiments to a minimum of 0.75 mg/cm^2 this will provide an aerial capacity of 2 mAh/cm^2 competitive with commercial high capacity electrodes.[37][38] Based on the capacity and capacity fade highlighted above, two varieties of porous sample are of interest. Low purity samples such as that reduced at 550 °C and high purity, such as 850 °C sample. It is envisaged that future work on electrode/electrolyte formulation and carbon coating will only increase the cyclability and initial CE of these materials.

These results demonstrate the complex nature of using porous silicon produced via MgTR as an anode material. Our results suggest that silica removal from the silicon product is not necessary and that it can be beneficial for the stability of silicon produced. The interplay of purity and pore properties in these samples is crucial. Purity most significantly affects the capacity reached, high purities reach higher capacities. Higher purities require porous structure to buffer silicon volume expansion upon cycling, larger mesopores are better able to mitigate the stresses of volume change.

3. CONCLUSIONS

Magnesiothermic reduction is a hard templating synthesis method which can be used to produce porous silicon from silica templates. However, poor characterisation of the precursor silica and silicon products as well as lack of understanding of the role of processing conditions has led to little understanding of how the MgTR process produces porous silicon.[7] We have found that although the macrostructure of the silica templates can be maintained through magnesiothermic reduction, the pore structure of the porous silicon is determined by the arrangement of free space between the silicon nanocrystallites formed. The maximum

temperature of the reduction is the driving factor of nanocrystallite sintering, as these nanocrystllites sinter the average pore sizes increases. The stoichiometry of the reactants is also a key factor determining the purity of the porous silicon formed. The side reaction reduces the purity of samples via the formation of Mg_2Si; the formation and removal of Mg_2Si is shown to broaden pore size distribution in the silicon product. We show that the reduction reaction reaches a thermodynamic equilibrium after 1 hour of reaction and that only by increasing the temperature, the purity of the samples can be increased. This purity increase is driven by the solid-state reduction of silica with magnesium silicide. The effect of larger silicon crystallites formed leads to larger pores between crystallites and at higher temperatures >850 °C the degradation of the BIS secondary particle structure. Applying these mechanistic insights, we demonstrated the formation of mesoporous silicon from previously non-porous quartz silica. This sample consolidates our theory that the formation of mesopores are between silicon nanocrystallites formed. The reduction of a variety of silica precursors showed an increase in silicon purity and sintering of nanocrystallite sizes at higher reduction temperatures, in turn this leads to an increase in pore size across the study.

The anode performance demonstrates the multifaceted nature of using porous silicon produced via MgTR as an anode material. The interplay of purity and pore properties in these samples is crucial. Higher purity, high capacity samples require porous structure to buffer silicon volume expansion upon cycling otherwise suffer from rapid capacity fade. With the detailed reaction design pathway for MgTR we have outlined, particularly the porous nature of these samples, future work can be more systematically applied to produce silicon products with targeted properties. Furthermore, the easily obtained crystallite size can be used to provide a quality control indicator as to the porous nature of the product. This mechanistic understanding to produce porous silicon via MgTR will find far reaching applications outside of the field LIBs.[7]

4. EXPERIMENTAL

4.1 Silica Preparation

BIS preparation: Sodium metasilicate (Sigma Aldrich) 31.8210g (0.15 moles) was dissolved into 4650ml of deionised water, inside of a 5L Radley's lab reactor. The solution is brought up to a mixing speed of 450rpm (identified as the critical mixing speed). Pentaethylene hexamine (PEHA) (Sigma Aldrich) 5.8093g (0.025 moles) was transferred to the 4650ml solution. A pH probe was used to measure the pH of the reaction mixture in-situ. Hydrochloric acid 1M (HCl) (Sigma Aldrich) 350ml (87.5 moles) was quickly added to the reaction mixture. The pH was monitored. Using a micro pipette addition HCl is added so the pH comes to rest at 7.00±0.05 within 2 minutes. After 5 minutes of reaction time, the product solution was collected from the bottom of the reactor. Vacuum filtration was used to removed unreacted species and separate out the silica. A minimum of 2 washes with deionised water was performed. Oven drying at 120°C for 24h followed by drying under vacuum at 120°C for 24h, completely dried the silica. The silica was calcined at 550°C under air for 5 hours to remove all organic additives. The resulting calcined silica was ball milled for 5 minutes to give a fine homogeneous powder.

Other silica sources were sourced from commercially available materials. Precipitated silica refers to Perkasil KS4080PD (Grace), Silica Gel refers to 'mesoporous silica gel 13nm' (Sigma), porous silica refers to microporous Syloid AL-1FP (Grace), Quarts was obtained as 'quartz white sand >99.995%' (Sigma).

4.2 Magnesiothermic reduction

In an argon glove box (MBraun), magnesium powder -325 mesh (Sigma Aldrich) was weighed into a pestle, the chosen silica powder was weighed into the pestle in an order to achieve a desired Mg:SiO_2 stoichiometric ratio. The two powders were ground thoroughly and evenly together. The reactants were transferred to the reactor (Figure S 17) and evenly distributed within before transferring the reactor to a tube furnace (Carbolite) which was then purged with argon. The furnace was then ramped at 5°C/min to 400 °C then 1°C/min to the desired temperature for a set time. Once cooled overnight in argon the powder sample was slowly

added to 1M HCl (Sigma Aldrich). The solution was left mixing for 48 hours. The remaining silicon powder was filtered through a Buckner funnel with a 450nm cellulose filter paper and washed with deionised water. The silicon was dried and stored in a 120 ^{o}C vacuum oven.

N.B. Preparation of the reactants was achieved by mortar and pestle grinding of stoichiometric amounts of silica and magnesium powders. Thorough mixing in this way achieved a homogenous distribution of magnesium and BIS. The respective sizes of the magnesium and BIS particles are, <44µm mesh and 300nm respectively. The smaller silica particles are therefore aggregated and spread evenly between the larger magnesium particles. The low vapour pressure and melting point of magnesium allow the magnesium to become mobile during the reduction and react with BIS particles that are not in direct contact.[7]

4.3 Electrode and Cell Preparation

A 2.5w% solution of carboxymethyl cellulose (Sigma) binder and deionised water was prepared. The desired solid amount of binder 20w% in electrode was added to a thinky mixer 10ml pot. The conductive additive C-65 (MTI) 20w% of electrode was added to the thinky. The mixer was sealed and mixed at 1500rpm for 5 minutes. The silicon was added to the mixer and mixed together for a further 10 minutes to give a viscous ink. The ink was transferred to a 10ml Perspex ball mill vial and milled in a Spex M8000 Mill with a stainless steel baring for 10 minutes. This ink was then applied to a carbon coated copper foil (MTI) using a vacuum table (MTI)and doctor blade with thickness 300 micrometers. The coating was air dried for 1-2 hours then placed in an 80^{o}C vacuum for a minimum of 6 hours. Once dry 12mm diameter electrodes are punched from the foil, weighed, and used for cell preparation. Electrochemical experiments were performed using MIT2016-type coin cells with a Whatman glass fibre separator and lithium foil (Sigma Aldrich) as the counter electrode. The electrolyte was 1M $LiPF_6$ in a 1:1 solution of ethylene carbonate (EC) and dimethyl carbonate (DMC) (Sigma Aldrich) with added 5w% fluoroethylene carbonate (FEC) (VWR). The composition of working electrodes was: 60w% silicon active material, 20w% conductive additive C-65, 20w% carboxymethyl cellulose. The mass loading if silicon active material was between 0.3-0.5

mg/cm^2. The commercial silicon nanoparticle size was <100nm from IOLiTech. The cells where assembled in an Argon filled glove box (MBraun) with oxygen and water contents less than 0.1ppm.

4.4 Materials Characterisation

XRD patterns were collected using a STOE STADI IP diffractometer in transmission mode. Cu $k_{\alpha 1}$ radiation wavelength 1.5406Å was selected for diffraction collection and patterns collected by an image plate detector. A total of 5 patterns were collected over the 2θ range of 1-100° for 5 minutes each. Diffraction patterns were combined before analysis. Scherrer analysis was performed in WinXPow software using integral breadths vs a polycrystalline silicon standard.

Silicon content was determined by thermo-gravimetric analysis performed in Air. The full oxidation of silicon to silica in air was achieved under heating to 1000°C for 24 hours. Full oxidation of silicon results in 114% weight gain, any deviation from this value allows evaluation of the initial silica concentration.

SEM images were taken on a FEI Inspect F50 scanning electron microscope. Samples were dispersed into dilute solutions of ethanol with sonication, then pipetted onto the carbon tabs and allowed to dry before analysis. Images were taken with 20kV accelerating voltage with SE detector.

Samples for N_2 absorption/desorption were degassed at 120°C under vacuum for minimum 12 hours before measurement. Analysis gas was N_2 with free space being measured with Ar using a Micromeritics 3Flex. The sample analysis ran from relative pressures of 0.01 to 0.998. Isotherms were fitted with the BET model for surface area and BJH on the desorption branch for mesopores volume using Micromeritics software.

USAXS studies were carried out at beamline 9 ID-C at the Advanced Photon Source, a U.S. Department of Energy (DOE) Office of Science User Facility by Argonne National Laboratory. This instrument is operated and maintained by Jan Ilavsky and his team.[39][40] Data reduction was performed using NIKA and IRENA packages in IGOR Pro.[41][42] Sauter

Mean diameter was taken as level 1 particle size and the radius of gyration (R_g) as an indication of level 2 particle size.

The electrochemical performances were tested on a Maccor 4000M Battery and Cell test system in a 25°C temperature chamber. The cut off voltage was 0.01V versus Li/Li^+ for discharge (lithium insertion) and 1.2V versus Li/Li^+ for charging (Li extraction). The specific capacity was calculated on the basis of active material mass. The charging rate was calculated from the fraction of active material in the electrode and based on silicon's' theoretical capacity at 25 °C of 3600mAh/g. When testing the rate capabilities of silicon containing electrodes the purity of the active material was considered. Such that for a sample with 50 wt% silicon at a C-rate of 0.1 the electrode experienced a current density of 0.18 A/g.

ACKNOWLEDGEMENTS

The authors thank EPSRC for funding (EP/L016818/1, EP/P006892/1 and EP/R041822/1) and the Fulbright Scholar Award. This research used resources of the Advanced Photon Source, a U.S. Department of Energy Office of Science User Facility operated for the DOE Office of Science by Argonne National Laboratory under Contract No. DE-AC02-06CH11357. The USAXS data was collected by Jan Ilavsky and his team at the X-ray Science Division. We would also like to acknowledge the vital assistance of Alex McGlasson, Michael Chauby, and Kabir Rishi from the Chemical and Materials Engineering department at the University of Cincinnati in conducting the x-ray scattering experiments.

REFERENCES

[1] M. M. Thackeray, C. Wolverton, E. D. Isaacs, *Energy Environ. Sci.* **2012**, *5*, 7854.
[2] M. N. Obrovac, L. J. Krause, *J. Electrochem. Soc.* **2007**, *154*, A103.
[3] R. Ruffo, S. S. Hong, C. K. Chan, R. A. Huggins, Y. Cui, *J. Phys. Chem. C* **2009**, *113*, 11390.
[4] N. Dimov, K. Fukuda, T. Umeno, S. Kugino, M. Yoshio, *J. Power Sources* **2003**, *114*, 88.
[5] M. Park, X. Zhang, M. Chung, G. B. Less, A. Marie, *J. Power Sources* **2010**, *195*, 7904.
[6] M. Ge, J. Rong, X. Fang, C. Zhou, *Nano Lett.* **2012**, *12*, 2318.
[7] J. Entwistle, A. Rennie, S. Patwardhan, *J. Mater. Chem. A* **2018**, *6*, 18344.
[8] J. Christensen, J. Newman, *J. Solid State Electrochem.* **2006**, *10*, 293.
[9] X. Zhang, W. Shyy, A. Marie Sastry, *J. Electrochem. Soc.* **2007**, *154*, S21.
[10] Y. Yao, M. T. McDowell, I. Ryu, H. Wu, N. Liu, L. Hu, W. D. Nix, Y. Cui, *Nano Lett.* **2011**, *11*, 2949.
[11] X. Li, M. Gu, S. Hu, R. Kennard, P. Yan, X. Chen, C. Wang, M. J. Sailor, J. Zhang, J. Liu, *Nat. Commun.* **2014**, *5*, 1.
[12] M. Ge, X. Fang, J. Rong, Chongwu Zhou, *Nanotechnology* **2013**, *24*.
[13] M. Ge, Y. Lu, P. Ercius, J. Rong, X. Fang, M. Mecklenburg, C. Zhou, *Nano Lett.* **2014**, *14*, 261.

[14] E. K. Richman, C. B. Kang, T. Brezesinski, S. H. Tolbert, *Nano Lett.* **2008**, *8*, 3075.
[15] D. Chung, E. Elgqvist, S. Santhanagopalan, *Clean Energy Manuf. Anal. Cent.* **2016**, DOI 10.2172/1333041.
[16] R. A. Rapp, A. Ezis, G. J. Yurek, *Metall. Trans.* **1973**, *4*, 1283.
[17] J. Liang, X. Li, Z. Hou, W. Zhang, Y. Zhu, Y. Qian, *ACS Nano* **2016**, *10*, 2295.
[18] M. Barati, S. Sarder, A. McLean, R. Roy, *J. Non. Cryst. Solids* **2011**, *357*, 18.
[19] H. Wu, N. Du, X. Shi, D. Yang, *J. Power Sources* **2016**, *331*, 76.
[20] J. R. H. Manning, E. Routoula, S. V Patwardhan, *JoVE* **2018**, e57730.
[21] S. V Patwardhan, *Chem. Commun. (Camb).* **2011**, *47*, 7567.
[22] C. Drummond, R. Mccann, S. V Patwardhan, *Chem. Eng. J.* **2014**, *244*, 483.
[23] S. V Patwardhan, V. P. Taori, M. Hassan, N. R. Agashe, J. E. Franklin, G. Beaucage, J. E. Mark, S. J. Clarson, *Eur. Polym. J.* **2006**, *42*, 167.
[24] J. R. H. Manning, T. W. S. Yip, A. Centi, M. Jorge, S. V. Patwardhan, *ChemSusChem* **2017**, *10*, 1683.
[25] S. V Patwardhan, J. R. H. Manning, M. Chiacchia, *Curr. Opin. Green Sustain. Chem.* **2018**, *12*, 110.
[26] N. Liu, K. Huo, M. T. McDowell, J. Zhao, Y. Cui, *Sci. Rep.* **2013**, *3*, 1.
[27] K. K. Larbi, M. Barati, a McLean, *Can. Metall. Q.* **2011**, *50*, 341.
[28] Z. Favors, W. Wang, H. H. Bay, Z. Mutlu, K. Ahmed, C. Liu, M. Ozkan, C. S. Ozkan, *Sci. Rep.* **2014**, *4*, 5623.
[29] C. Li, C. Liu, W. Wang, Z. Mutlu, J. Bell, K. Ahmed, R. Ye, M. Ozkan, C. S. Ozkan, *Sci. Rep.* **2017**, 1.
[30] H. Wu, Y. Cui, *Nano Today* **2012**, *7*, 414.
[31] X. H. Liu, L. Zhong, S. Huang, S. X. Mao, T. Zhu, J. Y. Huang, *ACS Nano* **2012**, *6*, 1522.
[32] K. Ogata, E. Salager, C. J. Kerr, A. E. Fraser, C. Ducati, A. J. Morris, S. Hofmann, C. P. Grey, *Nat. Commun.* **2014**, *5*, 3217.
[33] C. C. Nguyen, B. L. Lucht, *J. Electrochem. Soc.* **2014**, *161*, 1933.
[34] M. T. McDowell, S. W. Lee, W. D. Nix, Y. Cui, *Adv. Mater.* **2013**, *25*, 4966.
[35] S. Trask, P. Jennings, A. Mcgordon, C. Lyness, I. Bloom, **2016**, *335*, 189.
[36] D. Mazouzi, Z. Karkar, C. R. Hernandez, P. J. Manero, D. Guyomard, L. Roué, B. Lestriez, *J. Power Sources* **2015**, *280*, 533.
[37] S. D. Beattie, M. J. Loveridge, M. J. Lain, S. Ferrari, B. J. Polzin, R. Bhagat, R. Dashwood, *J. Power Sources* **2016**, *302*, 426.
[38] V. L. Chevrier, L. Liu, B. Le, J. Lund, B. Molla, K. Reimer, L. J. Krause, L. D. Jensen, E. Figgemeier, K. W. Eberman, *Electrochem. Soc.* **2014**, *161*, 3.
[39] J. Ilavsky, F. Zhang, A. J. Allen, L. E. Levine, P. R. Jemian, G. G. Long, *Metall. Mater. Trans. A* **2012**, *44A*, 68.
[40] J. Ilavsky, F. Zhang, R. N. Andrews, I. Kuzmenko, P. R. Jemian, L. E. Levine, A. J. Allen, *J. Appl. Crystallogr.* **2018**, *51*, 867.
[41] J. Ilavsky, P. R. Jemian, *J. Appl. Crystallogr.* **2009**, 347.
[42] J. Ilavsky, *J. Appl. Crystallogr.* **2012**, *45*, 324.

SUPPLEMENTARY INFORMATION

Parameter study

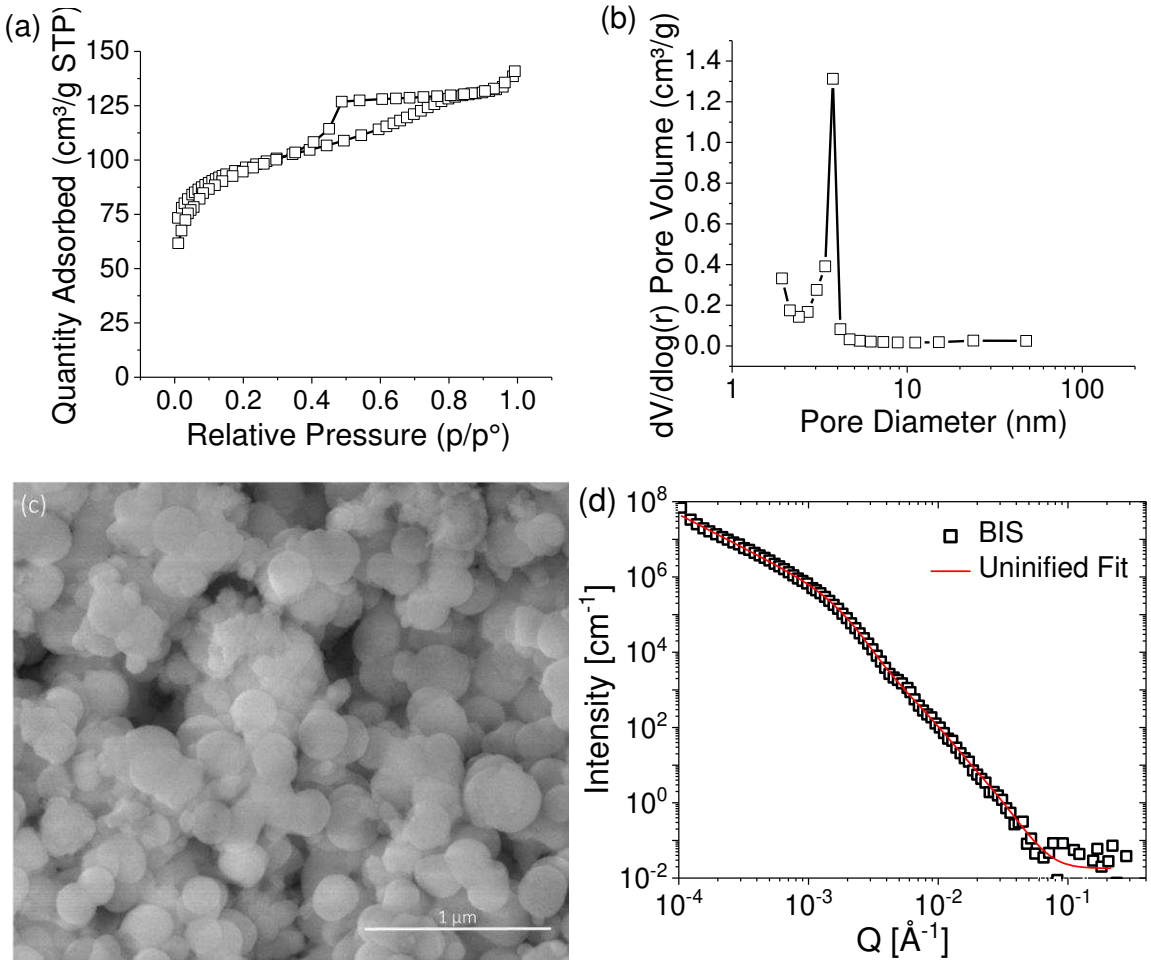

Figure S 1, characterisation of BIS*, (a) N_2 absorption Isotherm, (b) BJH pore size distribution, (c) SEM image, (d)USAXS data obtained for BIS along with unified fit.*

Table S 1. Materials properties of BIS

	BET SSA (m^2/g)	BJH PV (cm^3/g)	USAXS Particle Size	
			Level1 (nm)	level 2 (nm)
Bioinspired PEHA	301	0.16	26	370

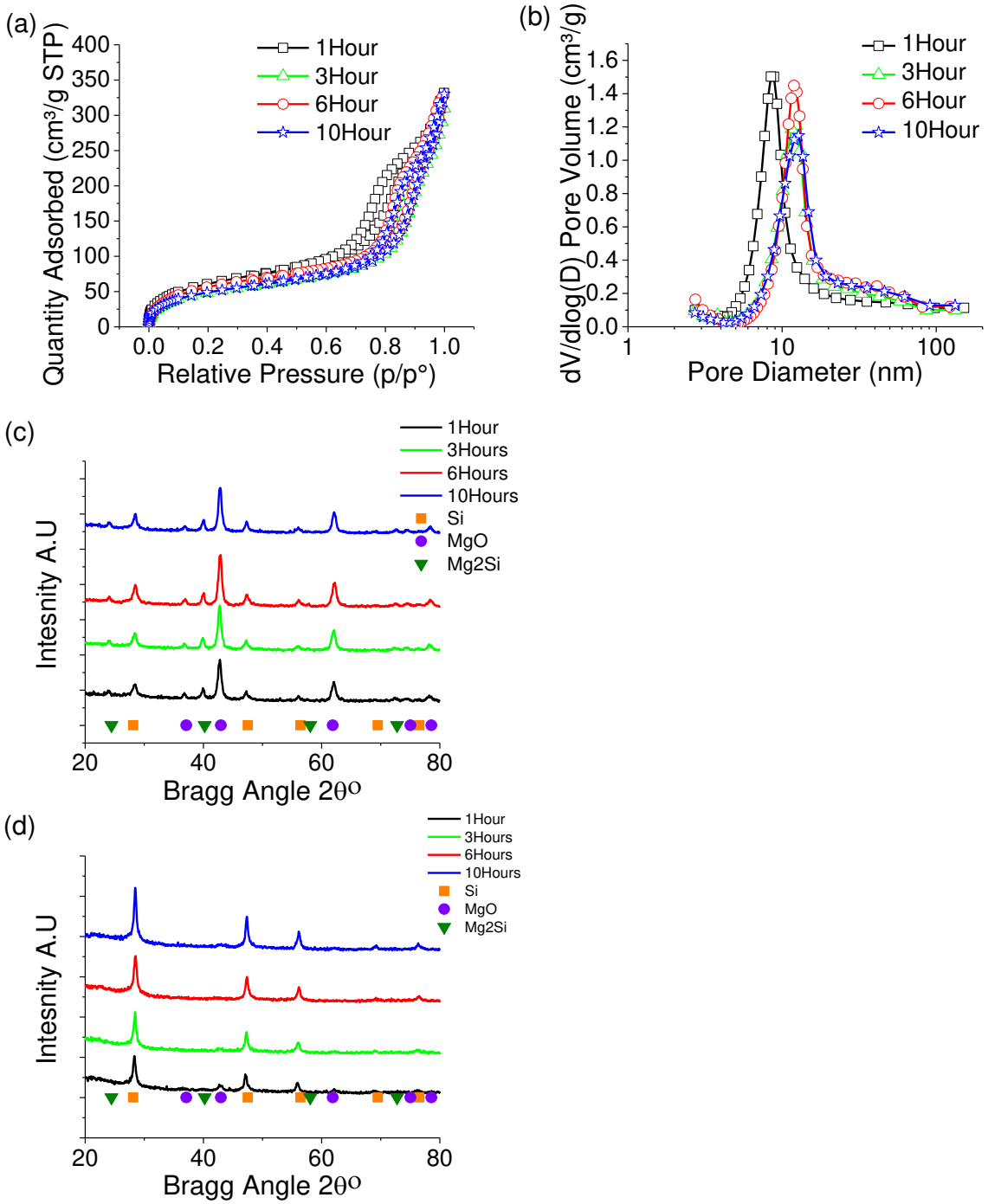
(a)
Quantity Adsorbed (cm³/g STP)
Relative Pressure (p/p°)
1Hour
3Hour
6Hour
10Hour
(b)
dV/dlog(D) Pore Volume (cm³/g)
Pore Diameter (nm)
1Hour
3Hour
6Hour
10Hour
(c)
Intesnity A.U
Bragg Angle 2θº
1Hour
3Hours
6Hours
10Hours
Si
MgO
Mg2Si
(d)
Intesnity A.U
Bragg Angle 2θº
1Hour
3Hours
6Hours
10Hours
Si
MgO
Mg2Si

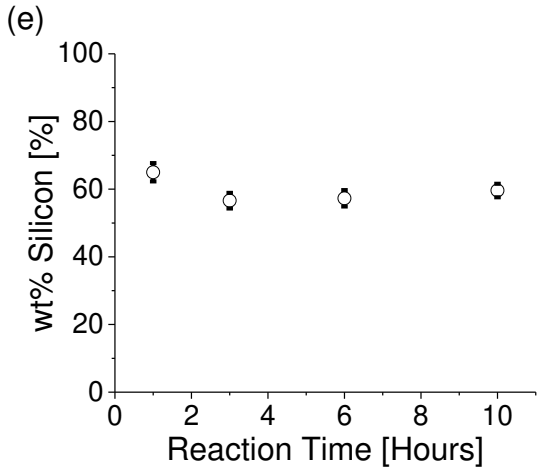

Figure S 2. Characterisation of silicon produced during kinetic study of, 2.5:1 Mg:SiO_2 stochimetry reacted between 1 and 10 hours at 650 °C. (a) N_2 absorption Isotherm, (b) BJH pore size distribution, (c) XRD of reaction products before washing with HCl, (d) XRD of reduction products after washing with HCl, (e) purity of silicon samples.

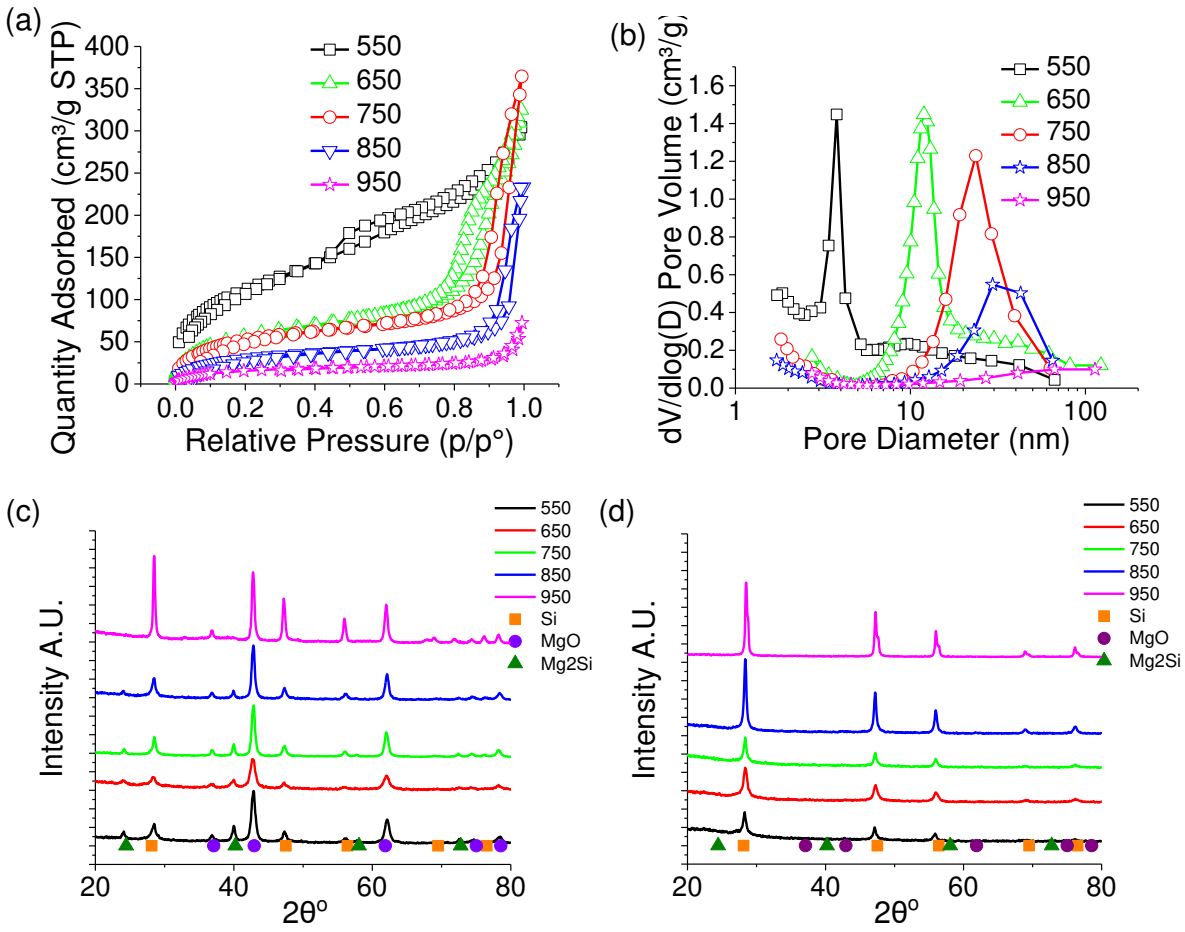

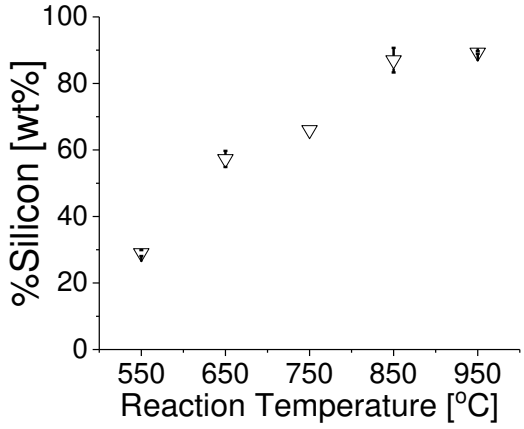

Figure S 3. Characterisation of silicon produced during thermodynamic study of 2.5:1 Mg:SiO2 stoichiometry reacted for 6 hours between temperatures of 550-950 °C. (a) N2 absorption Isotherm, (b) BJH pore size distribution, (c) XRD of reaction products before washing with HCl, (d) XRD of reduction products after washing with HCl, (e) purity of silicon sample.

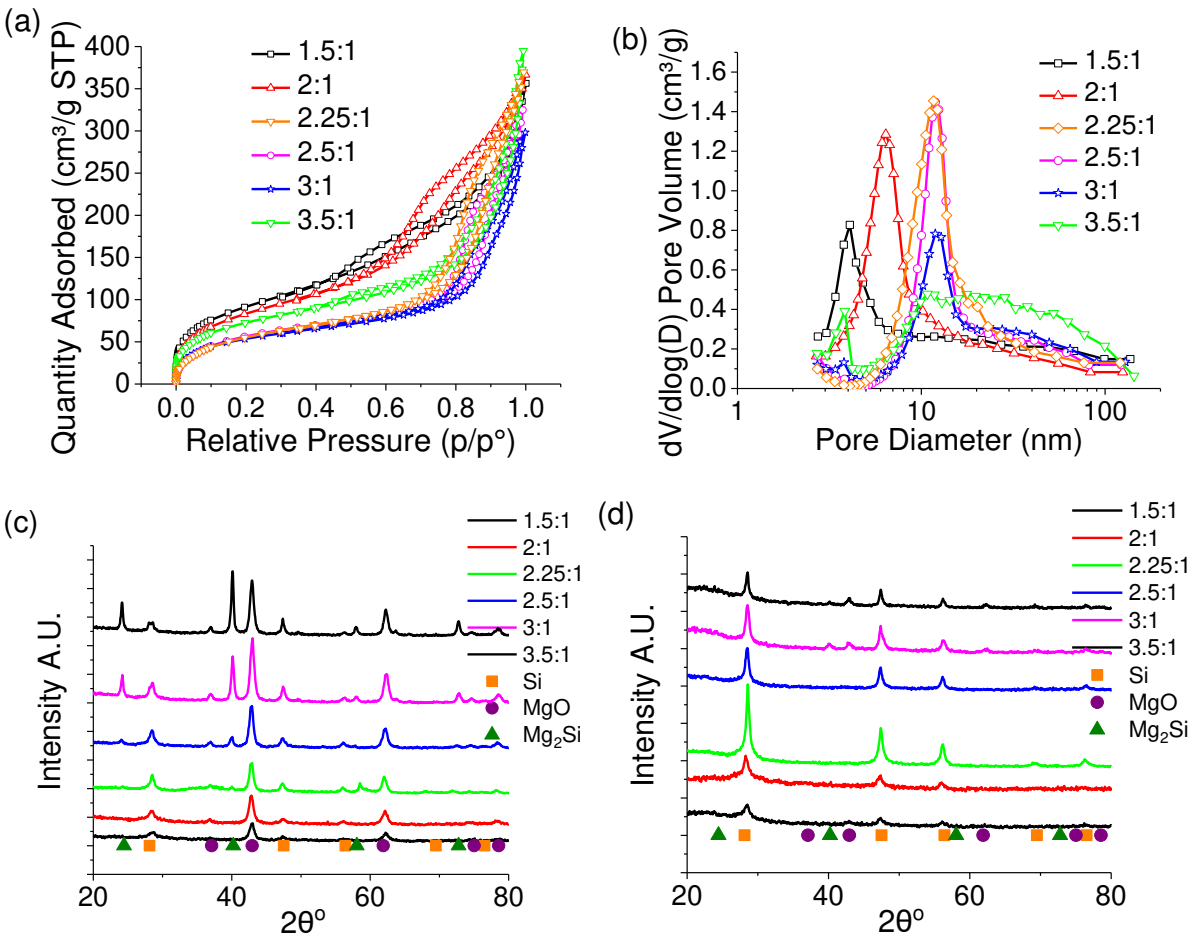

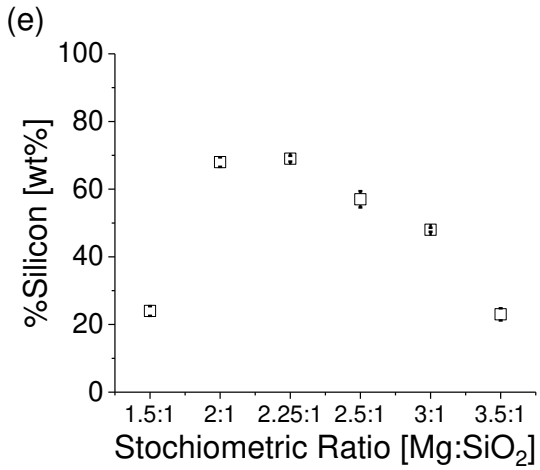

Figure S 4. Characterisation of silicon produced during stoichiometric study for stoichiometries between 1.5-3.5:1 Mg:SiO2 reacted for 6 hours at 650 °C. (a) N2 absorption Isotherms, (b) BJH pore size distributions, (c) XRD of reaction products before washing with HCL, (d) XRD of reduction products after washing with HCl, (e) purity of silicon samples.

Table S 2. Summary of Figure S 2 for the kinetic study of, 2.5:1 Mg:SiO2 stoichiometry reacted between 1 and 10 hours at 650°C

Reaction Time (h)	BET SSA (m^2/g)	BJH PV (cm^3/g)	APD (nm)	wt% Si	Si_{Cry} Size (nm)
1	232	0.50	10	65	12
3	181	0.46	13	57	11
6	221	0.48	13	57	10
10	186	0.49	14	60	12

Table S 3. Summary of Figure S 3 for the thermodynamic study of, 2.5:1 Mg:SiO2 stoichiometry reacted 6 hours at temperatures between 550 and 950°C

Reaction Temp (°C)	BET SSA (m^2/g)	BJH PV (cm^3/g)	APD (nm)	wt% Si	Si_{Cry} Size (nm)	USAXS Particle Size	
						Level 1 (nm)	Level 2 (nm)
550	402	0.48	4	29.0	5	25.84	413
650	230	0.48	12	57.3	10	40.28	208
750	185	0.54	13	66.0	13	49.85	333
850	110	0.35	34	87.0	21	16.94	323

950	65	0.10	-	89.3	48	24.86	645

-outside of BJH model range

Table S 4. summary of Figure S 4 for the stoichiometric study of, Mg:SiO2 stoichiometry between 1.5-3.5:1 Mg:SiO2 reacted 6 hours at 650 °C

Stoichiometric Ratio ($Mg:SiO_2$)	BET SSA (m^2/g)	BJH PV (cm^3/g)	APD (nm)	wt% Si	Si_{Cry} Size (nm)
1.5:1	340	0.50	4	24	11
2.0:1	315	0.55	6	68	6
2.25:1	217	0.56	12	69	10
2.5:1	230	0.48	13	57	10
3.0:1	206	0.43	12*	48	9
3.5:1	271	0.57	28*	23	15

*Bimodal distribution so representative of pore size distribution, see Figure S 4(b)

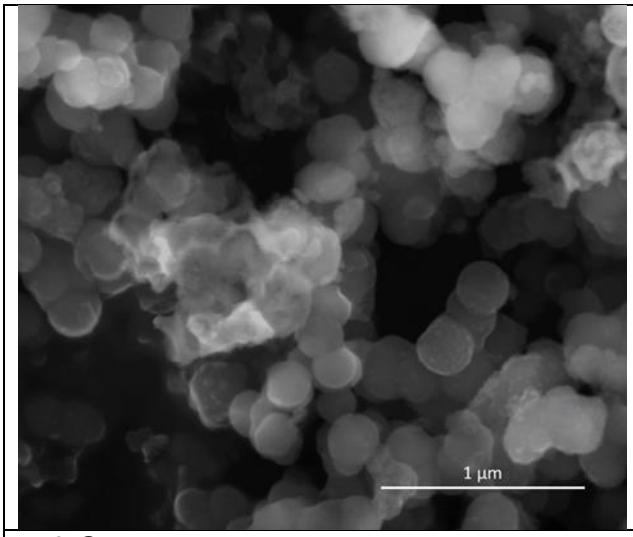

550°C

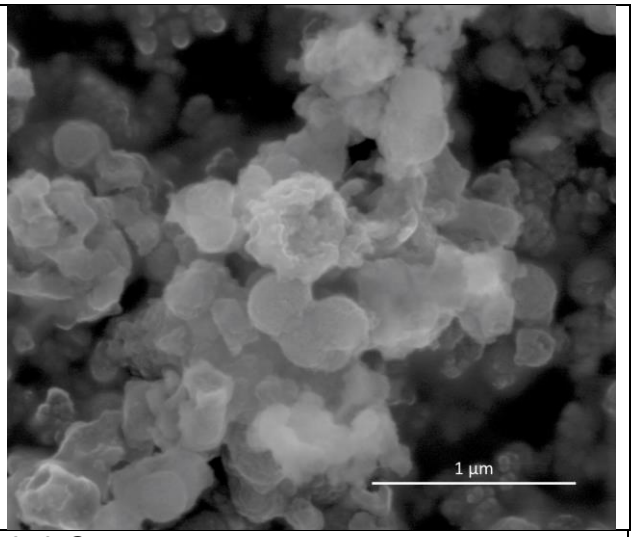

650°C

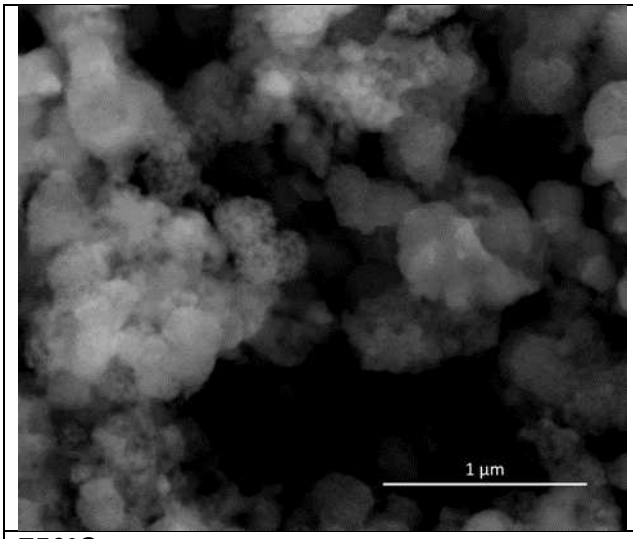

750ºC

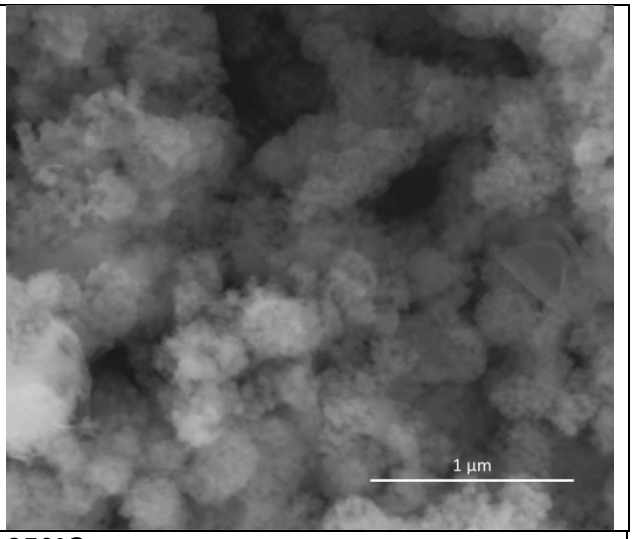

850ºC

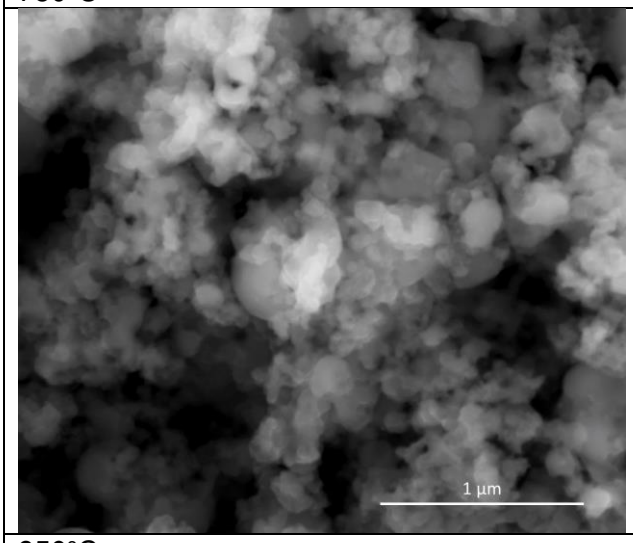

950ºC

Figure S 5, SEM images of BIS *reduced at temperatures 550 – 950ºC.*

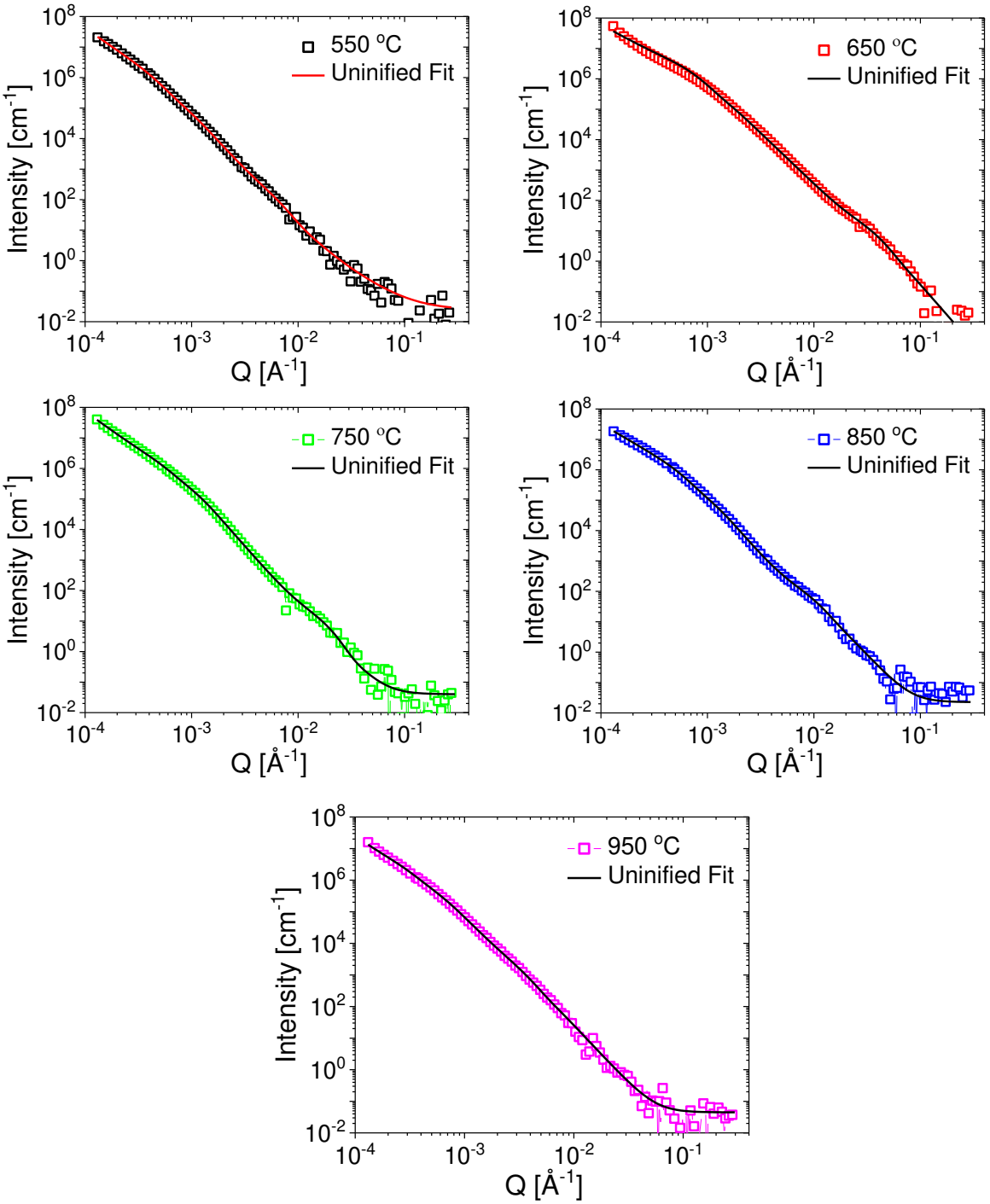

Figure S 6, USAXS data of porous silicon reduced at temperatures between 550-950 °C. Not all data points shown for clarity.

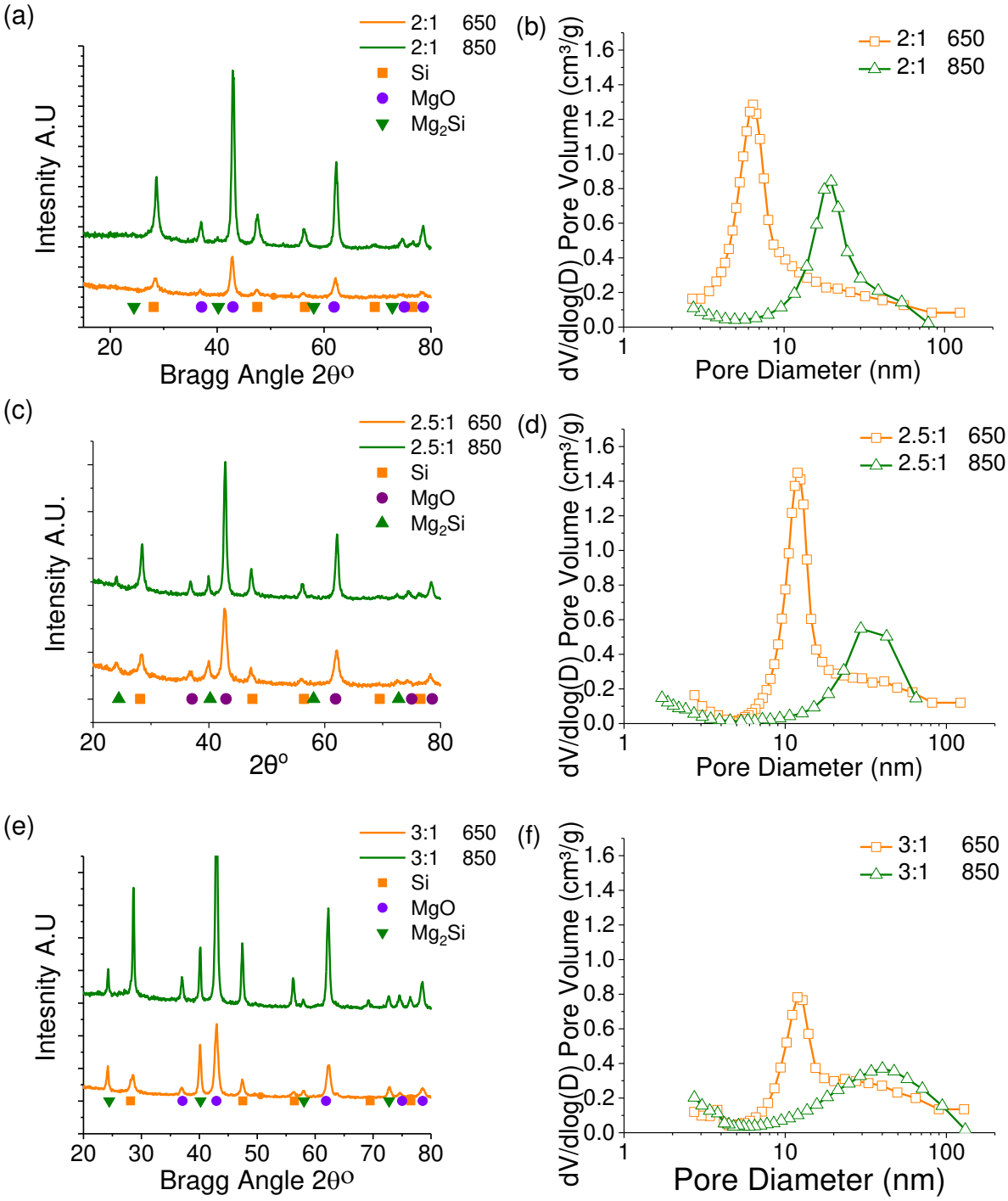

Figure S 7. Silicon/silica composites reduced at 650 and 850 °C with 2:1, 2.5:1 and 3:1 stoichiometric ratios of Mg:SiO2. (a,c,e) Diffraction patterns of after acid washing. (b,d,f) BJH pore size distributions.

Table S 5, summary of Figure S 7 .

Sample	Reduction Temp (°C)	BET SSA (m^2/g)	BJH PV (cm^3/g)	APD (nm)	wt% Si	Si_{Cry} Size (nm)
2:1	650	315	0.55	7	68	6
2:1	850	130	0.35	20	83	10
2.5:1	650	230	0.48	12	57	10
2.5:1	850	110	0.35	34	87	21
3:1	650	206	0.48	12	48	9
3:1	850	152	0.32	45	78	30

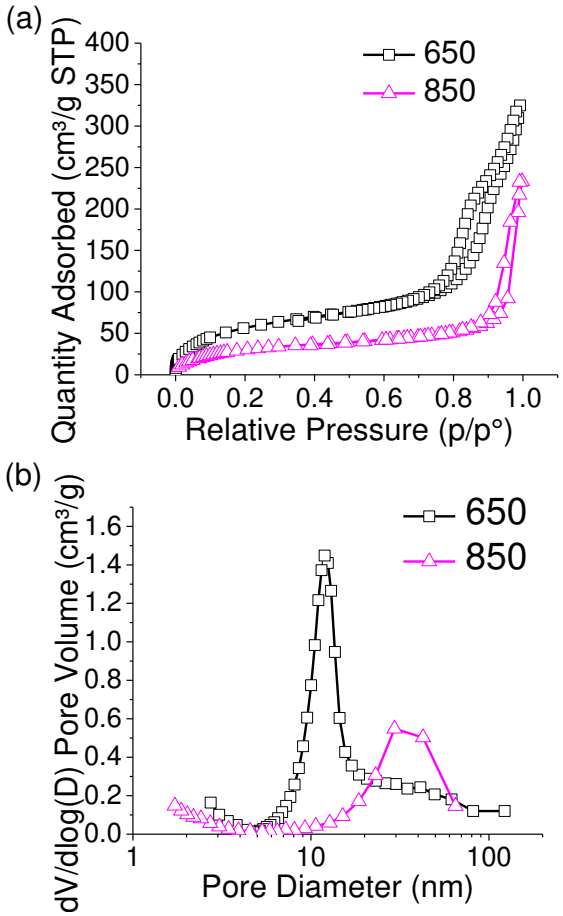

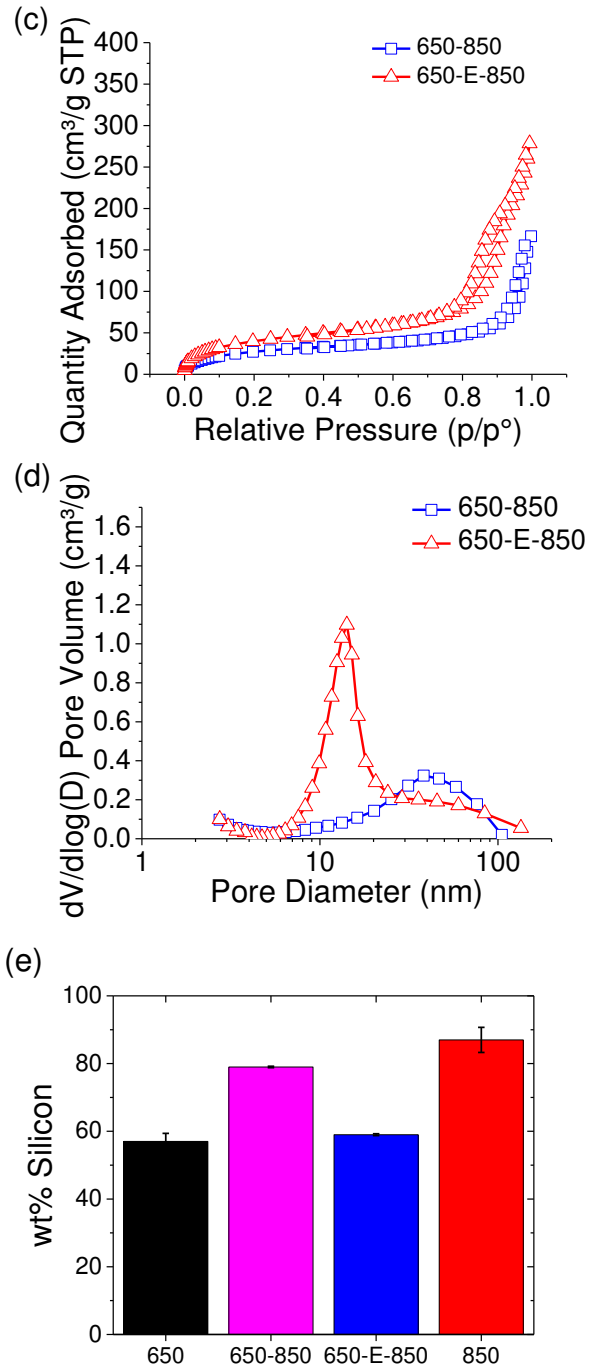

Figure S 8. Characterisation of samples used to understand the thermodynamic evolution of the MgTR *reaction, samples include silicon reduced at 650 and 850°C, Silicon reduced at 650 °C washed in HCl acid then heated to 850 °C under argon (650-E-850), and silicon reduced at 650 °C allowed to cool then reheated to 850°C (650-850). (a)(c) N_2 absorption Isotherms, (b)(d) BJH pore size distributions, (e) purity of silicon samples.*

Silica Precursors

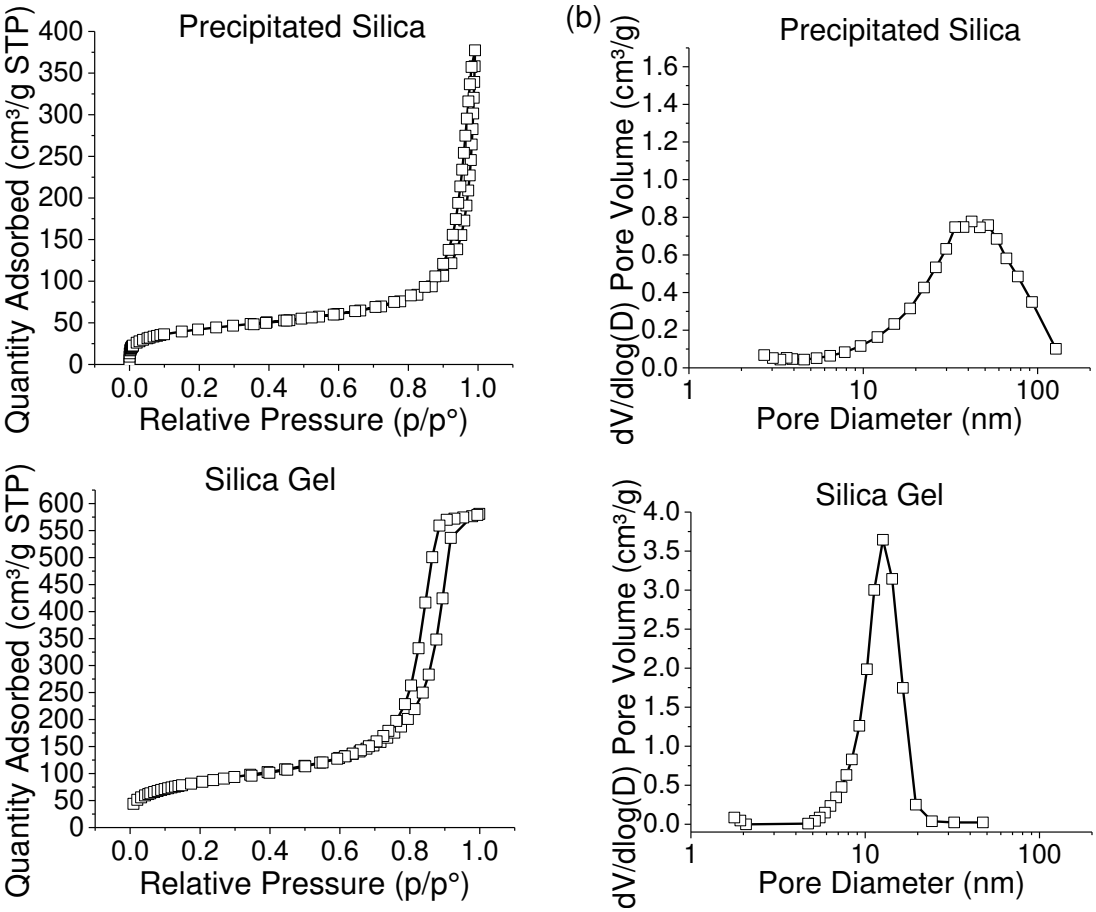

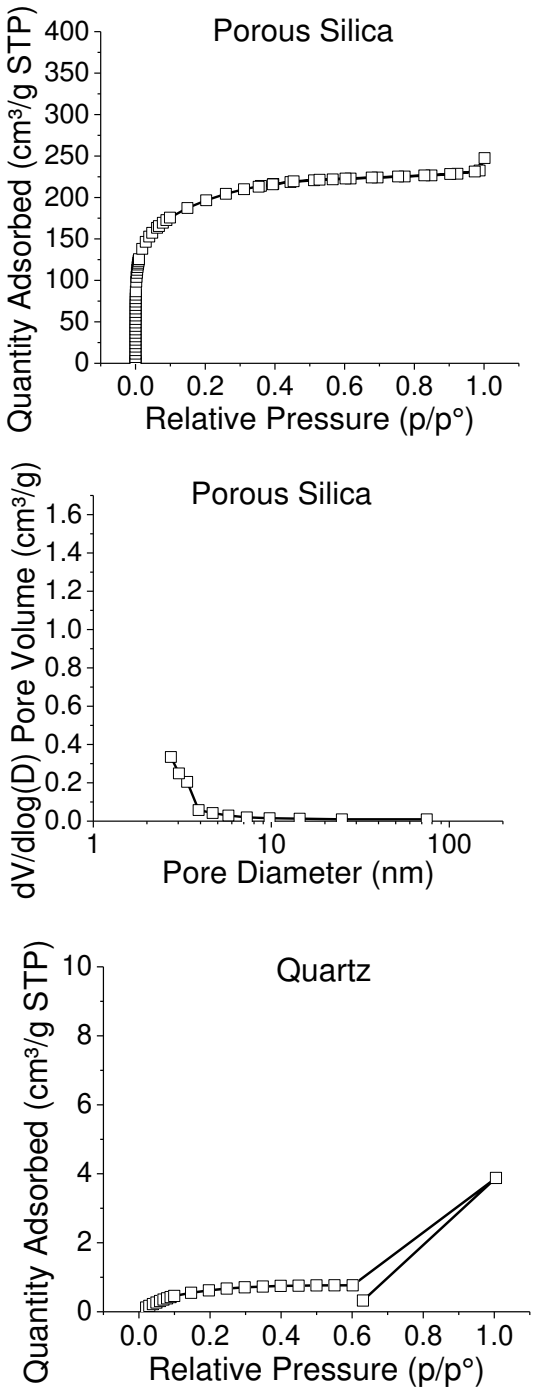

Figure S 9, N_2 absorption Isotherms and BJH pore size distributions of silica sources.

Table S 6.SSA, BJH pore volume, purity and crystallite size of silicon reduced at 650 and 850 °C for different silica precursors.

Precursor	Reduction Temperature (°C)	BET SSA (m^2/g)	BJH PV (cm^3/g)	wt% Si	Si_{Cry} Size (nm)
Ppt. silica		156	0.56		
Ppt. silica	650	220	0.63	56.3	9
Ppt. silica	850	108	0.40	60.9	19
Silica Gel		264	0.89		
Silica Gel	650	275	0.73	50.7	6
Silica Gel	850	158	0.48	80.3	13
BIS		301	0.16		
BIS	650	216	0.48	57.3	10
BIS	850	110	0.35	87.0	21
Porous SiO_2		725	0.09		
Porous SiO_2	650	205	0.45	41.9	22
Porous SiO_2	850	90	0.27	79.4	28
Quartz	Non-porous				
Quartz	650	310	0.36	31.1	17
Quartz	850	76	0.30	85.2	26

Reduced Products

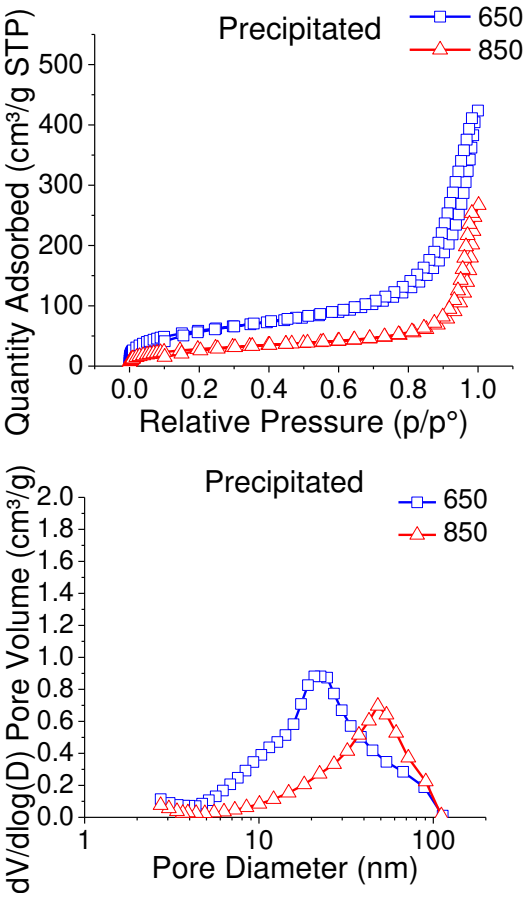

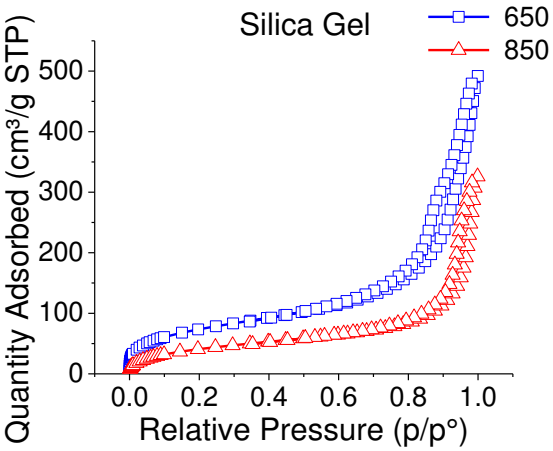
Silica Gel
650
850
Quantity Adsorbed (cm³/g STP)
0
100
200
300
400
500
0.0
0.2
0.4
0.6
0.8
1.0
Relative Pressure (p/p°)

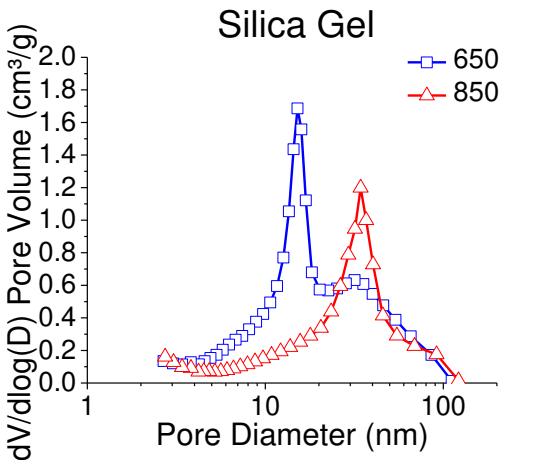
Silica Gel
650
850
dV/dlog(D) Pore Volume (cm³/g)
0.0
0.2
0.4
0.6
0.8
1.0
1.2
1.4
1.6
1.8
2.0
1
10
100
Pore Diameter (nm)

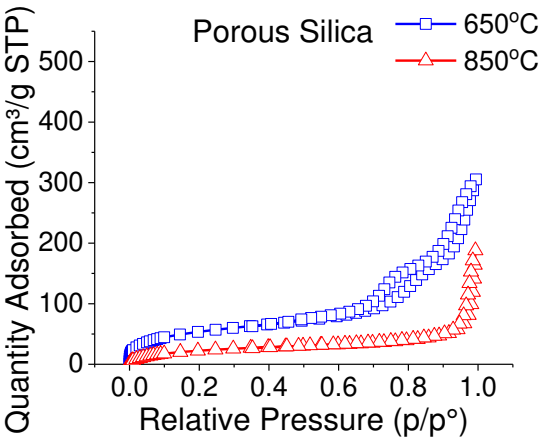
Porous Silica
650°C
850°C
Quantity Adsorbed (cm³/g STP)
0
100
200
300
400
500
0.0
0.2
0.4
0.6
0.8
1.0
Relative Pressure (p/p°)

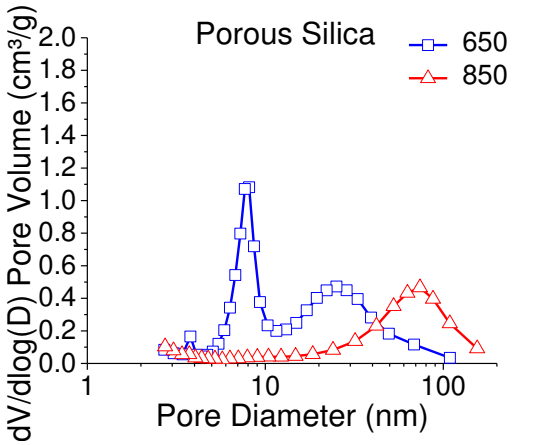
Porous Silica
650
850
dV/dlog(D) Pore Volume (cm³/g)
0.0
0.2
0.4
0.6
0.8
1.0
1.2
1.4
1.6
1.8
2.0
1
10
100
Pore Diameter (nm)

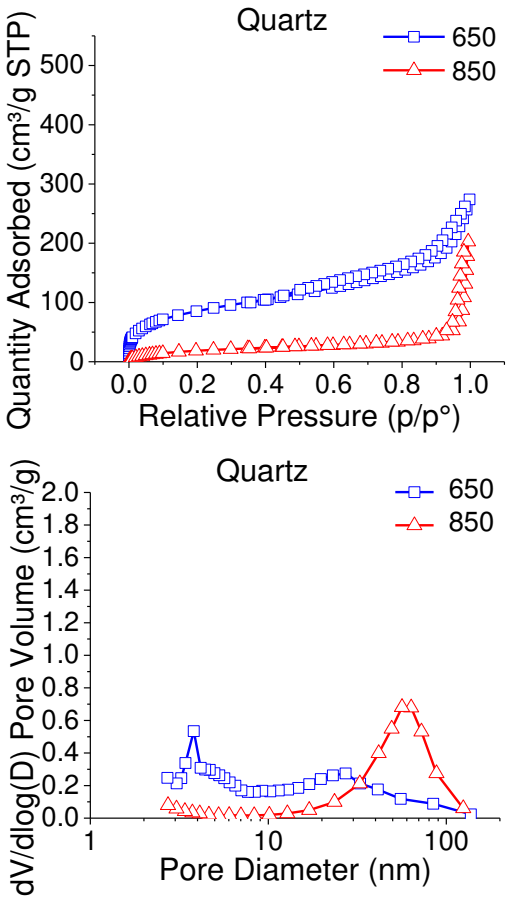

Figure S 10. N_2 absorption Isotherms and BJH pore size distributions of silicon reduced from variety of silica sources at 650 and 850 °C.

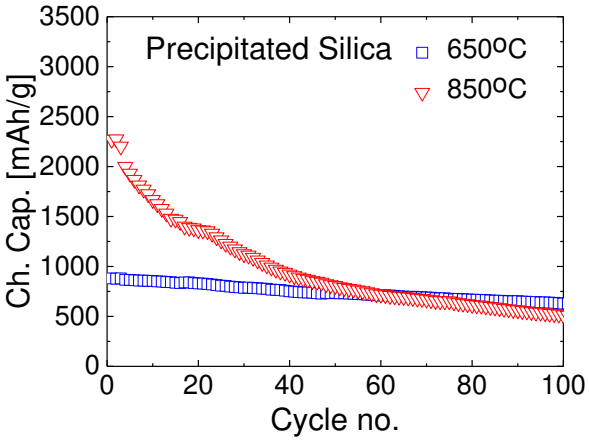
Precipitated Silica
650ºC
850ºC
Ch. Cap. [mAh/g]
Cycle no.
0
500
1000
1500
2000
2500
3000
3500
0
20
40
60
80
100

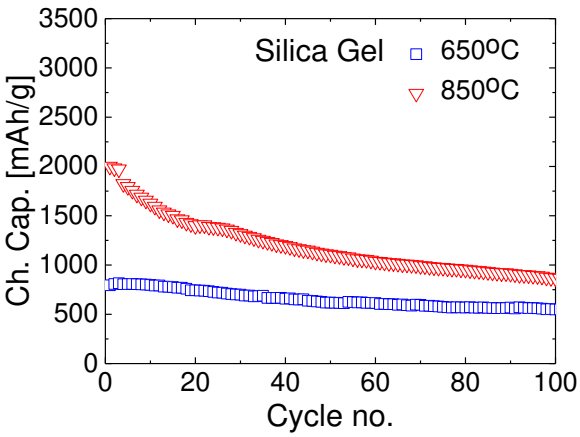
Silica Gel
650ºC
850ºC
Ch. Cap. [mAh/g]
Cycle no.
0
500
1000
1500
2000
2500
3000
3500
0
20
40
60
80
100

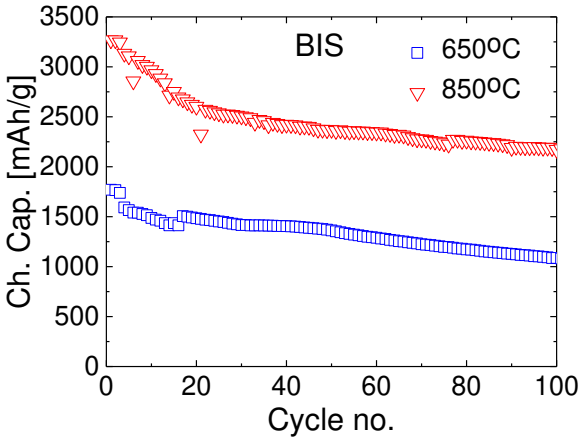
BIS
650ºC
850ºC
Ch. Cap. [mAh/g]
Cycle no.
0
500
1000
1500
2000
2500
3000
3500
0
20
40
60
80
100

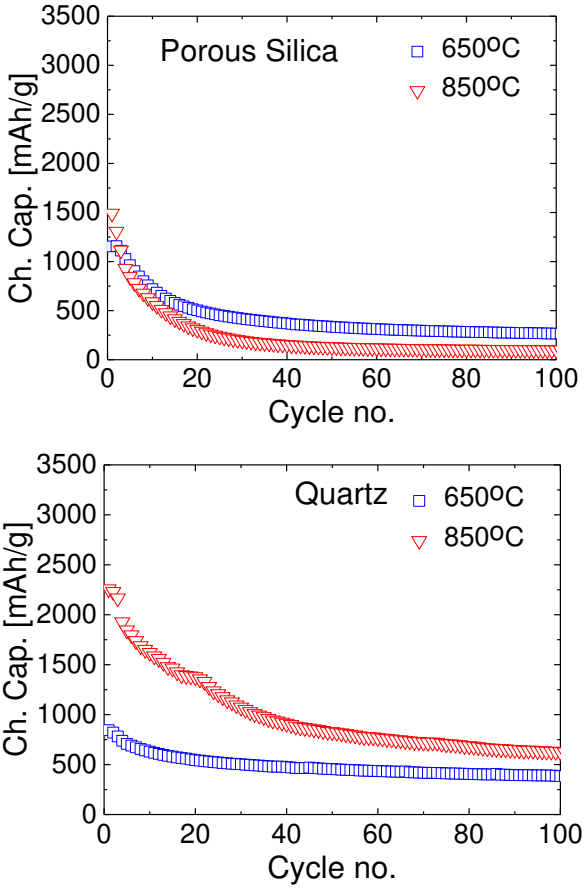

Figure S 11. Discharge capacity of porous silicon/silica composites reduced at 650 and 850 °C

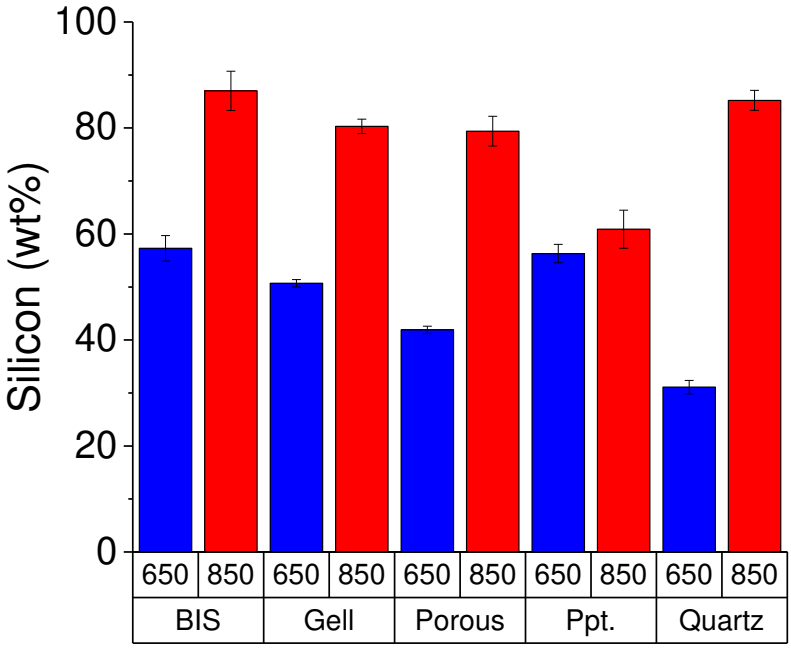

Figure S 12. Purity of silicon reduced from silica sources at 650 and 850 °C

Anode performance

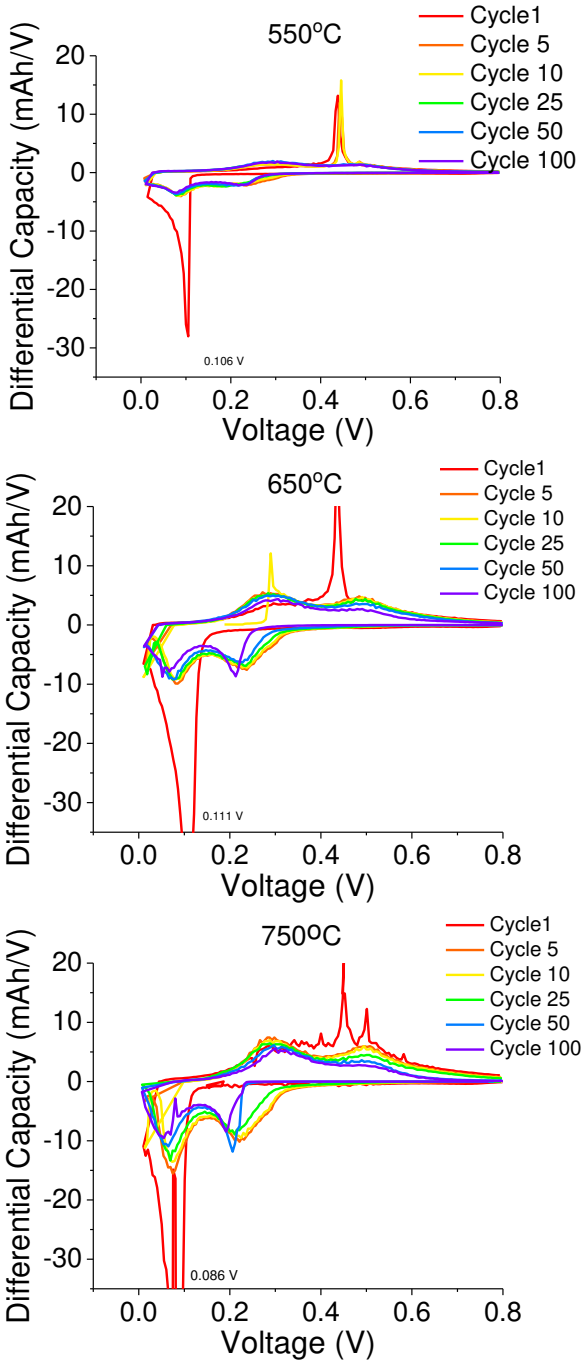

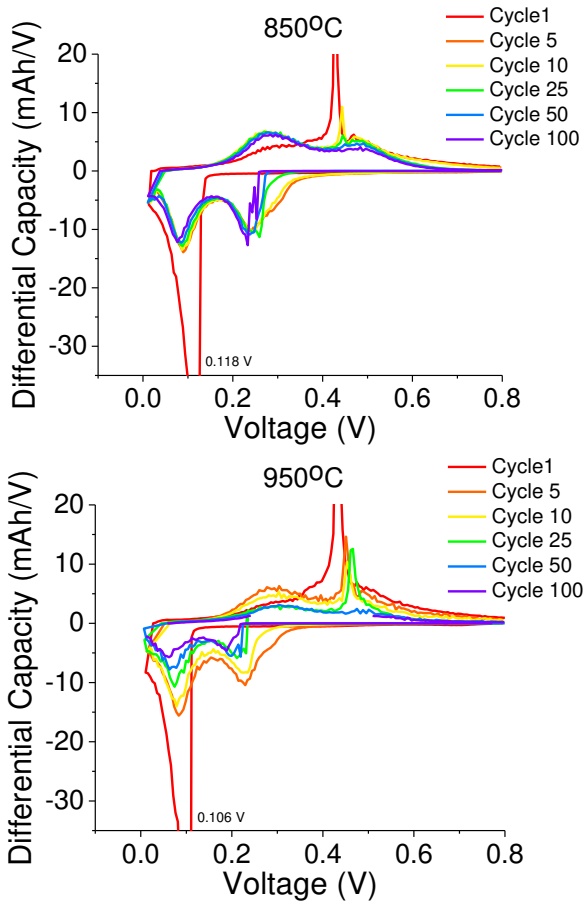

Figure S 13. Differential capacity plots of the 1st, 5th, 10th, 25th, 50th and 100th cycles for silicon reduced between 550-950 ºC

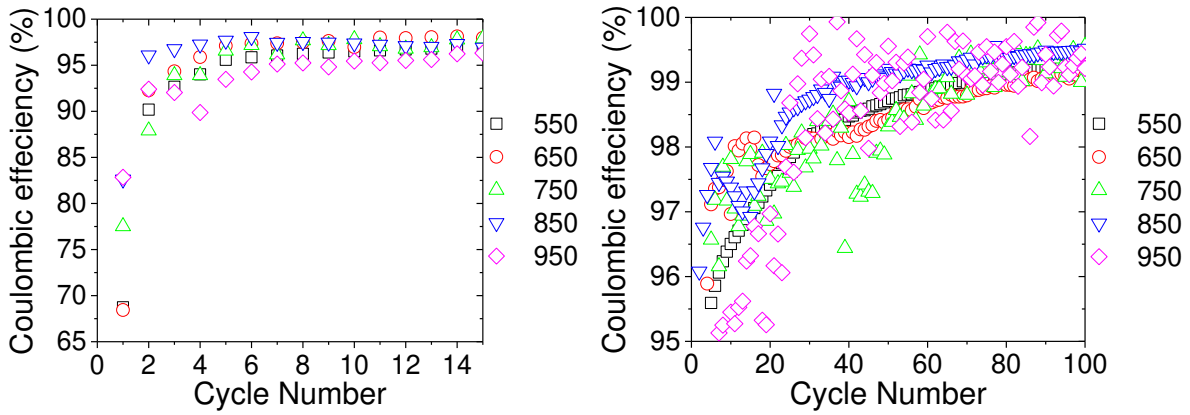

Figure S 14. Columbic efficiencies (a) during the first 10 cycles, (b) for 100 cycles of silicon's reduced at 550-950 ºC

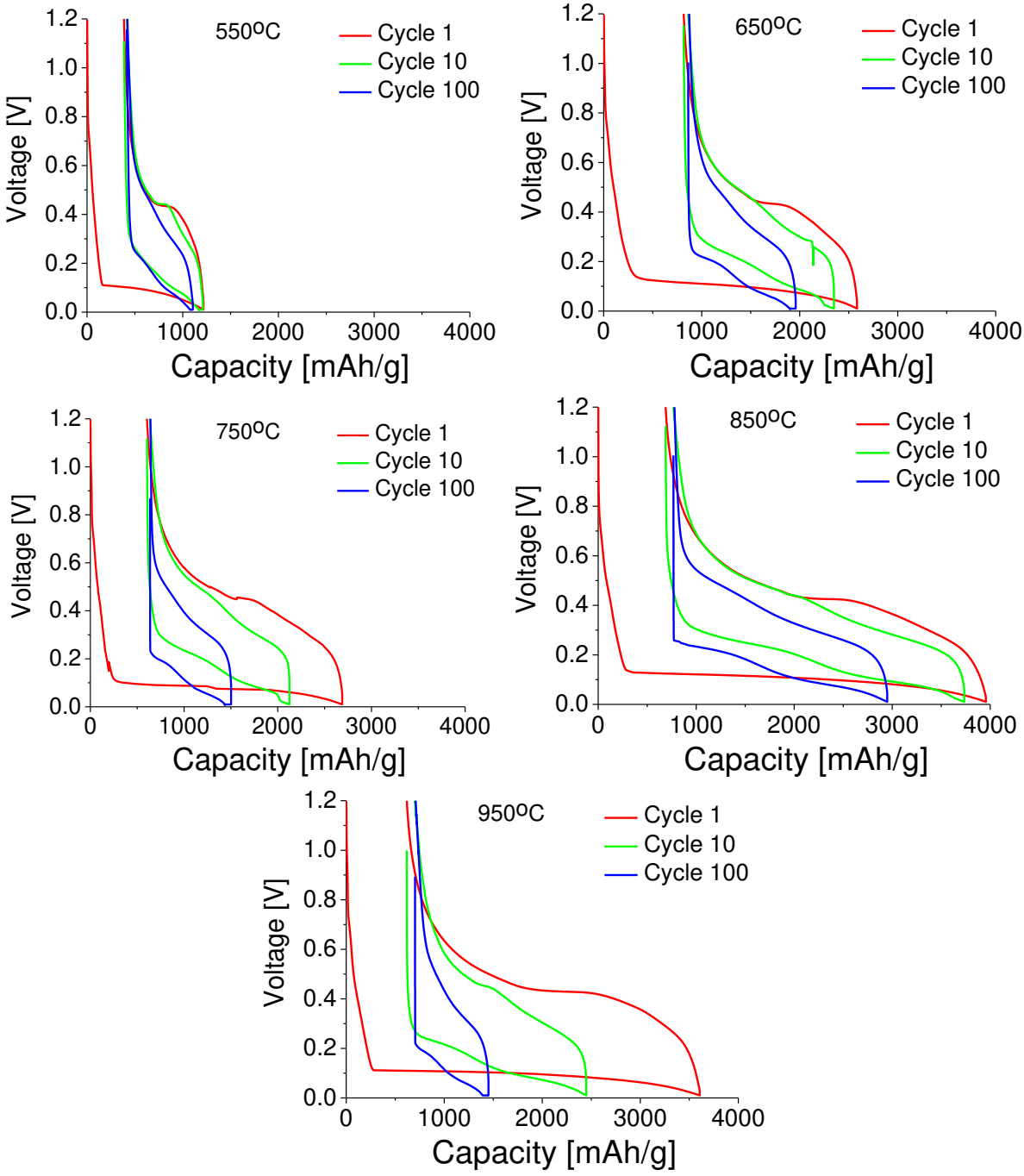

Figure S 15. Voltage capacity profiles of the 1st, 10th and 100th cycles for silicon reduced from 550-950 °C

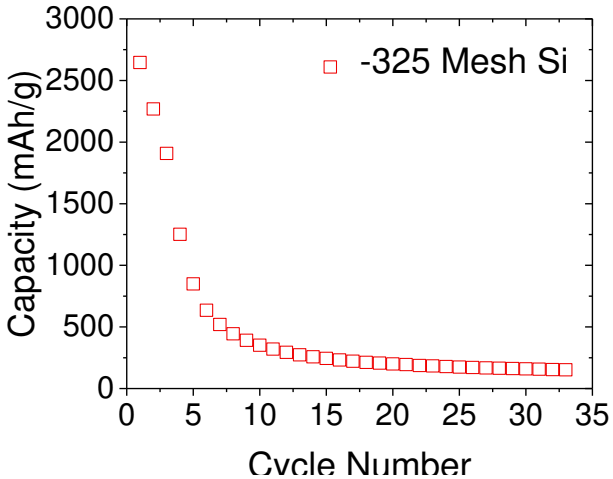

Figure S 16. Capacity vs cycle life of micron sized silicon particles (-325 mesh)

Figure S 17. Steel trough reactor with lid used in this study.